Modeling the Formation and Composition of Secondary Organic Aerosol from Diesel Exhaust Using Parameterized and Semi-Explicit Chemistry and Thermodynamic Models

Sailaja Eluri[1], Christopher D. Cappa[2], Beth Friedman[3], Delphine K. Farmer[3], and Shantanu H. Jathar[1]

[1] Department of Mechanical Engineering, Colorado State University, Fort Collins, CO, USA, 80523

[2] Department of Civil and Environmental Engineering, University of California Davis, Davis, CA, USA, 95616

[3] Department of Chemistry, Colorado State University, Fort Collins, CO, USA, 80523

Correspondence to: Shantanu H. Jathar (shantanu.jathar@colostate.edu)

Abstract

Laboratory-based studies have shown that combustion sources emit volatile organic compounds that can be photo-oxidized in the atmosphere to form secondary organic aerosol (SOA). In some cases, this SOA can exceed direct emissions of primary organic aerosol (POA). Jathar et al. (2017) recently reported on experiments that used an oxidation flow reactor (OFR) to measure the photochemical production of SOA from a diesel engine operated at two different engine loads (idle, load), two fuel types (diesel, biodiesel) and two aftertreatment configurations (with and without an oxidation catalyst and particle filter). In this work, we used two different SOA models, the volatility basis set (VBS) model and the statistical oxidation model (SOM), to simulate the formation and composition of SOA for those experiments. Leveraging recent laboratory-based parameterizations, both frameworks accounted for a semi-volatile and reactive POA; SOA production from semi-volatile, intermediate-volatility, and volatile organic compounds (SVOC, IVOC and VOC); NO_X-dependent parameterizations, multigenerational gas-phase chemistry; and kinetic gas/particle partitioning. Both frameworks demonstrated that for model predictions of SOA mass to agree with measurements across all engine load-fuel-aftertreatment combinations, it was necessary to model the kinetically-limited gas-particle partitioning in OFRs as well as account for SOA formation from IVOCs, which were on average found to account for 70% of the model-predicted SOA. Accounting for IVOCs however resulted in an average under-prediction of 28% for OA atomic O:C ratios. Model predictions of the gas-phase organic compounds (resolved in carbon and oxygen space) from the SOM compared favorably to gas-phase measurements from a Chemical Ionization Mass Spectrometer (CIMS), substantiating the semi-explicit chemistry captured by the SOM. Model-measurement comparisons were improved on using vapor wall-loss corrected SOA parameterizations. As OFRs are increasingly used to study SOA formation and evolution in laboratory and field environments, models such as those developed in this work can be used to interpret the OFR data.

1 Introduction

Combustion-related aerosols are an important contributor to urban and global air pollution and have impacts on climate (Pachauri et al., 2014) and human health (Anderson et al., 2012). While direct particle emissions from combustion sources are dominated by primary organic aerosol (POA) and black carbon (Bond et al., 2004), these sources also emit more volatile organic compounds (VOCs) that can photochemically react in the atmosphere to form secondary organic aerosol (SOA) (Robinson et al., 2007). SOA production from combustion emissions is poorly understood and not very well represented in models in terms of its precursors, gas-particle partitioning, composition, and properties (Fuzzi et al., 2015). Atmospheric models frequently under-predict SOA mass concentrations during strong photochemical episodes in urban areas (Jathar et al., 2017b), which likely highlights the challenge in modeling the SOA contributions from urban, combustion-related emissions (Ensberg et al., 2014).

Diesel-powered sources, which are an important source of air pollution at urban and regional scales, emit precursors that form SOA in the atmosphere (Gentner et al., 2016). Robinson et al. (2007) found that photochemical processing of exhaust emissions from a small off-road diesel engine led to SOA production and doubled the primary aerosol mass over a few hours in an environmental chamber. Chirico et al. (2010) and Gordon et al. (2014) performed similar chamber experiments on tailpipe emissions from in-fleet, on-road diesel vehicles run on chassis dynamometers. Both found SOA production that was roughly consistent with the findings from Robinson et al. (2007). They additionally found that the use of aftertreatment devices (diesel oxidation catalysts and diesel particulate filters) substantially reduced SOA production (mimicking the reduction in primary aerosol emissions) but observed some SOA production during cold starts and/or regeneration events when the proper functioning of the aftertreatment devices was limited. Furthermore, Gordon et al. (2014) found negligible differences in the SOA formation between diesel and biodiesel fuel. To access longer equivalent photochemical aging timescales compared to typical chamber experiments, Tkacik et al. (2014) measured SOA formation using an oxidation flow reactor (OFR) from air sampled from a highway tunnel in Pittsburgh, PA used by both on-road gasoline and diesel vehicles. OFRs use high concentrations of atmospheric oxidants, e.g. hydroxyl radicals, to achieve long exposures on short actual timescales; further discussion is provided below. Tkacik et al. (2014) measured much stronger SOA formation compared to chambers (SOA: POA was 10:1) over photochemical exposures equivalent to 2 to 3 days, but found that the SOA was lost, or destroyed, as the mixture continued to age over the timescale of a week. Recently, Jathar et al. (2017a) performed experiments using an oxidation flow reactor to measure the photochemical production of SOA from an off-road diesel engine operated at various engine load, fuel, and aftertreatment configurations. Jathar et al.

69   (2017a) found that efficient combustion at higher engine loads and removal of SOA precursors by

70   aftertreatment systems reduced SOA production by factors of 2 to 10. The only exception was that the

71   aftertreatment system did not seem to reduce SOA production at idle loads possibly because the exhaust

72   temperatures were low enough to limit removal of SOA precursors in the oxidation catalyst. Overall,

73   these studies indicate that diesel exhaust contributes to atmospheric SOA production, although the precise

74   production of SOA varies across dimensions of photochemical age, engine duty cycle, use of alternative

75   fuels, and aftertreatment devices.

76

77   Oxidation flow reactors are being used to study the photochemical production of SOA from both

78   anthropogenic (e.g., Ortega et al. (2016)) and natural (e.g., Palm et al. (2016)) sources. Most OFRs used

79   for SOA studies are 10 to 15 L, flow-through metal reactors with lamps that can produce high

80   concentrations of atmospheric oxidants to simulate photochemical processing (e.g., Lambe et al. (2011)).

81   Flows through an OFR allow for residence times between one and four minutes, but given the high

82   oxidant concentrations OFRs can simulate several weeks of photochemistry. OFRs have three distinct

83   advantages over environmental chambers. First, OFRs are smaller in size and easier to operate than

84   environmental chambers, which allows for shorter experiments and makes them ideal for field

85   deployments (Palm et al., 2016;Simonen et al., 2017). Second, production of high oxidant concentrations

86   in OFRs allows for much longer photochemical exposures (~factor of 10) than those possible with

87   chambers (Lambe et al., 2011). Third, due to their flow-through nature, OFRs have shorter residence

88   times than conventional chambers (~1-4 minutes) and hence are less susceptible to gas and particle losses

89   that can influence SOA formation (Zhang et al., 2014;Krechmer et al., 2016). Despite those advantages,

90   there are concerns that the accelerated chemistry and limitations to gas/particle partitioning may affect the

91   formation and composition of SOA in OFRs, which calls into question their relevance in understanding

92   SOA formation in the real atmosphere (Palm et al., 2016;Jathar et al., 2017a;Ahlberg et al., 2017). For

93   example, short residence times and/or small condensation sinks from preexisting aerosol may not allow

94   for complete condensation of SOA vapors (Lambe et al., 2015). Similarly, high oxidant concentrations in

95   OFRs may lead to molecules undergoing a greater number of reactions in the gas-phase before

96   condensing, including reactions that lead to fragmentation and formation of higher volatility products

97   (Kroll et al., 2009). Both effects will typically suppress SOA production. With the increased use of OFRs,

98   there is a need to develop and use modeling tools that can account for fragmentation reactions and kinetic

99   gas/particle partitioning. This will allow for a more accurate interpretation of OFR data and facilitate

100   translation of OFR results to the real atmosphere.

101

102   Models used to simulate the photochemical production of SOA from VOCs in combustion emissions have

103   traditionally used the two-product (Odum et al., 1996) or the more generalized n-product volatility basis

104   set (VBS) framework (Donahue et al., 2006a). In this framework, VOC oxidation products are lumped

105   into volatility bins based on their effective saturation concentrations (C*) and where the saturation

106   concentration determines the partitioning of the products between the gas and particle phases (Pankow,

107   1994). This framework has been widely used in both box (Dzepina et al., 2009;Hodzic et al., 2010;Jathar

108   et al., 2014a;Hayes et al., 2015) and three-dimensional (Murphy and Pandis, 2009;Tsimpidi et al.,

109   2009;Jathar et al., 2011;Ahmadov et al., 2012;Konovalov et al., 2015) models to simulate the chemistry

110   and gas/particle partitioning of SOA. While this framework offers a simple and computationally efficient

111   scheme to model SOA formation, the use of volatility alone neither tracks the molecular composition, nor

112   informs the continued multi-generational chemistry that will determine the atmospheric evolution and

113   properties of SOA. As a result, volatility-based models have been challenged in leveraging observations

114   of the elemental composition of SOA (e.g., atomic O:C ratios) that have become possible through the use

115   of the aerosol mass spectrometer (AMS) to constrain parameterizations or test model predictions. Further,

116   most volatility-based models have employed *ad hoc* parameterizations to model multi-generational

117   chemistry that do not account for fragmentation reactions (Robinson et al., 2007) and possibly double

118   count SOA formation (Jathar et al., 2016). Therefore, there is a demand to develop models that can

119   provide an improved representation of the chemistry that governs the formation, composition, and

120   properties of SOA.

121

122   Previously, volatility-based SOA models have been used to predict photochemical production of SOA

123   from motor vehicle exhaust (Robinson et al., 2007;Jathar et al., 2014b;Tkacik et al., 2014). These

124   modeling studies have shown that speciated SOA precursors such as long alkanes (C_{6-12}) and single-ring

125   aromatics (e.g., benzene, toluene) explain less than 20% of the observed SOA and have argued that the

126   remainder of the SOA (~80%) arises from the photooxidation of typically unspeciated organic

127   compounds. These unspeciated compounds, also referred to as intermediate volatility organic compounds

128   (IVOCs), are likely species with carbon numbers larger than 12 and appear as an unresolved complex

129   mixture on using traditional gas chromatography mass spectrometry (GC-MS) techniques (Presto et al.,

130   2011). Early estimates of IVOC emissions and their SOA potential have significantly improved

131   predictions of the SOA formed from diesel exhaust (Jathar et al., 2014b) and have broadly improved OA

132   model performance in three-dimensional large-scale models (Murphy and Pandis, 2009;Pye and Seinfeld,

133   2010;Jathar et al., 2011;Tsimpidi et al., 2009). Consider as an example that Zhao et al. (2015), using a

134   thermal desorption GC-MS to provide detailed speciation of the carbon-number resolved linear, branched,

and cyclic alkane IVOCs in diesel exhaust, found that these species accounted for up to 60% of the non-methane organic gas emissions. While IVOCs have been recognized as an important class of SOA precursors for diesel (and even for gasoline and biomass burning) sources, updated emissions and speciation estimates from Zhao et al. (2015) have not yet been used to explain observations of photochemically produced SOA from diesel exhaust.

Recently, several model frameworks have been developed to improve the representation of SOA formation, considering dimensions of SOA beyond just volatility. The statistical oxidation model (SOM) developed by Cappa and Wilson (2012) is one such example, although volatility remains an important consideration. The SOM is a semi-explicit, parameterizable mechanism that uses a two-dimensional carbon-oxygen grid to simulate the multigenerational chemistry and gas/particle partitioning of organic compounds. Although the SOM does not explicitly track or specify the product species composition (e.g., functional groups), the carbon- and oxygen-number representation provides adequate detail to represent many key atmospheric processes, e.g., reactions with oxidants, formation of functionalized products, scission of carbon backbones or fragmentation, surface and condensed-phase chemistry and gas/particle partitioning. The SOM has been used to interpret chamber experiments (Zhang et al., 2014; Cappa et al., 2013; Cappa and Wilson, 2012) and was recently integrated into a chemical transport model (Jathar et al., 2015) to examine the influence of multigenerational aging (Jathar et al., 2016) and chamber-based vapor wall losses (Cappa et al., 2016) on ambient concentrations and properties of OA. The two-dimensional VBS (2D-VBS) of Donahue et al. (2011) and the carbon-polarity grid of Pankow and Barsanti (2009) are examples of similar frameworks. These more sophisticated models (i.e., SOM, 2D-VBS, carbon-polarity grid) have not yet been employed to study SOA formation from complex mixtures such as combustion emissions.

To summarize, combustion sources such as diesel-powered sources emit precursors that can photooxidize in the atmosphere to produce SOA. This SOA production is dependent not only on the precursor composition (that could vary by combustion mode and fuel type) and photochemical age, but also experimental artifacts (e.g., short condensation timescales) introduced by oxidation flow reactors. Hence, there is a need to develop and apply sophisticated, yet computationally efficient, numerical models to simulate and study SOA formation from combustion emissions. In this work, we applied two SOA model frameworks that vary in sophistication (VBS and SOM) to simulate the photochemical production of SOA in an OFR from diesel exhaust. The models were evaluated by comparing model predictions (OA and O:C) to the recent measurements made by Jathar et al. (2017a) where SOA production was quantified for

168   different photochemical ages under varying engine loads, fuels, and aftertreatment devices. The model-

169   measurement comparison, along with sensitivity simulations, highlights the importance of modeling the

170   kinetic gas/particle partitioning of SOA in OFRs, the contribution of IVOCs to the total SOA production,

171   and the ability of the SOM to accurately track the composition of SOA.

172

173   **2 Methods**

174   **2.1 Experiments and Data**

175   Jathar et al. (2017a) performed photooxidation experiments using an OFR to measure SOA production

176   from the exhaust of a 4.5L, John Deere diesel engine. The stock engine met Tier 3 emissions standards for

177   off-road diesel engines. The OFR used therein was described in detail by Friedman et al. (2016) and the

178   experimental setup and OA measurements from these experiments were described in detail by Jathar et al.

179   (2017a). We briefly summarize the experimental setup, measurements, and findings from Jathar et al.

180   (2017a). The engine was run at two different loads (idle and 50% load) with two different fuels (diesel

181   and biodiesel), and with and without an aftertreatment system. The aftertreatment system included a diesel

182   oxidation catalyst (DOC) to oxidize CO and THC and a diesel particle filter (DPF) to trap fine particles.

183   Diesel exhaust was diluted by a factor of 45-110 before entering the OFR. The intensity of the mercury

184   lamps (at wavelengths of 185 and 254 nm) inside the OFR was varied to produce different hydroxyl

185   radical (OH) concentrations and simulate different photochemical exposures. The OFR had a residence

186   time of 100 s. A suite of instrumentation was used to measure gas- (CO_2, CO, total hydrocarbons, NO_x,

187   O_2, oxygenated organic compounds) and particle- (aerosol size and composition) phase concentrations. A

188   total of fourteen experiments (see Table 1 for more details) were performed at varying engine loads and

189   with varying fuels and aftertreatment configurations. The OH exposure was varied between 0 and a

190   maximum of 9.2×10^7 molecules-hr cm^{-3} (equivalent to 2 days of photochemical aging at an OH

191   concentration of 1.5×10^6 molecules cm^{-3}). On average, each experiment included measurements at six to

192   seven different photochemical exposures. The mass concentrations and elemental composition of the POA

193   (measured when OFR lights were off) and SOA (at varying OH exposures) were measured by a high-

194   resolution aerosol mass spectrometer (HR-AMS). In addition to the measurements reported by Jathar et al.

195   (2017a), the gas-phase concentrations of oxygenated organic compounds were measured by an acetate

196   reagent ion-based chemical ionization mass spectrometer (CIMS) (Link et al., 2016). At all engine

197   configurations, SOA production exceeded the POA emissions after the equivalent of a few hours of

198   atmospheric photochemical aging. SOA production was particularly strong at idle (or less fuel-efficient)

199   engine loads and/or when exhaust temperatures were low and proper functioning of the aftertreatment

200   devices was limited. Further, POA emissions and SOA production were nearly identical between diesel

201   and biodiesel fuels. A synopsis of experiments performed and the total hydrocarbons (THC), which

202   includes all SOA precursors, POA, SOA, O:C, OH, and size distribution data are presented in Table 1.

203

204   Although the diesel exhaust was diluted with clean air to produce atmospherically-relevant concentrations

205   of POA, the initial THC, CO, and NO_X concentrations in the OFR were still quite high. Peng and Jimenez

206   (2017), using a detailed gas-phase model, argued that the high external OH reactivity from high THC,

207   CO, and NO_X concentrations might lead to non-OH chemistry in the OFR and NO could quickly be

208   consumed in the OFR leading to low NO conditions for SOA formation. Peng and Jimenez (2017)

209   quantified the potential influence of NO on the oxidation chemistry by calculating the ratio of the reactive

210   flux of the peroxy radicals with NO to the reactive flux of the peroxy radicals with HO_2 ($r_{RO2+NO}/r_{RO2+HO2)}$.

211   A ratio greater than 1 was considered as "high NO" while a ratio less than 1 was considered "low NO".

212   For the relative humidity, photon flux, initial NO, and external OH reactivity values in Jathar et al.

213   (2017a), the model of Peng and Jimenez (2017) predicted that the OFR mostly ran in a high NO mode at

214   all photochemical exposures when the engine was run at load conditions or with an aftertreatment device

215   in place. However, the model predicted that the OFR mostly ran in a low NO mode especially at the high

216   photochemical exposures when the engine was run at idle conditions and without an aftertreatment device

217   (i.e., Idle-Diesel-None and Idle-Biodiesel-None). The $r_{RO2+NO}/r_{RO2+HO2}$ ratio and low versus high NO

218   mode for each photon flux-experiment combination is listed in Table S1. Based on these results, we

219   accordingly used the low and high NO_X parameterizations to perform the model simulations.

220

221   **2.2 Organic Aerosol Models**

222   In this work, we used two different OA models to predict the mass concentrations and chemical

223   composition of SOA and compare predictions against the SOA measurements from Jathar et al. (2017a)

224   and Friedman et al. (2017). In this section, we briefly describe the two model frameworks, namely the

225   Volatility Basis Set (VBS) and the Statistical Oxidation Model (SOM), used to simulate the coupled

226   chemistry, thermodynamic properties, and kinetic gas/particle partitioning of OA. The VBS model was

227   chosen as it is widely used in contemporary air quality models; the SOM was chosen to examine the

228   influence of improved representation of OA processes (e.g., fragmentation reactions) on model

229   predictions.

230

231   **2.2.1 Volatility Basis Set**

232   The Volatility Basis Set model, developed by Donahue et al. (2006b), is a parameterizable model that

233   allows for a volatility-based representation of the coupled chemistry, thermodynamic properties, and

234 gas/particle partitioning of OA. The VBS uses logarithmically spaced so-called basis sets based on the

235 effective saturation concentration (C^*); C^* of a species determines the partitioning between the gas and

236 particle phases (Pankow, 1994). In the VBS model, organic precursors were allowed to react with OH to

237 yield a unique product distribution in C^* space that represented stable first-generation products.

238 Subsequent multi-generational gas-phase oxidation, or so-called 'aging,' of the VBS products was

239 modeled using the scheme of Robinson et al. (2007). In this scheme the product species are allowed to

240 react with OH and yield a product with a C^* that is an order of magnitude lower than the direct precursor,

241 to a lower limit C^* of 10^{-2} µg m^{-3}. This scheme did not consider fragmentation reactions. The following

242 equations were used to represent the organic precursor oxidation (equation 1) and subsequent reaction and

243 formation of products from the precursor oxidation and aging reactions (equation 2):

244 $$\frac{dV}{dt} = -k_{OH}[V][OH] \tag{1}$$

245 $$\frac{dC_j^{g+p}}{dt} = \alpha_j k_{OH}[V][OH] + \beta\, k_{OH,aging}[C_{j+1}^g][OH] - \gamma\, k_{OH,aging}[C_j^g][OH] \tag{2}$$

246 where V is the gas-phase concentration of a generic organic precursor (µg m^{-3}; includes VOCs, IVOCs

247 and SVOCs), k_{OH} is the reaction rate constant between the precursor and OH (cm^3 molecule^{-1} s^{-1}), C_j^{g+p}

248 is the gas + particle-phase concentration in the jth bin (µg m^{-3}), α_j is the mass yield of the first-generation

249 oxidation product of the jth bin (Table 2), $k_{OH,aging}$ is the reaction rate constant (cm^3 molecule^{-1} s^{-1}) to

250 represent multi-generational aging of the oxidation products, and β and γ are the mass yields associated

251 with the production and loss terms from multi-generational aging. For the jth bin, the second term in

252 equation (2) represents the formation of oxidation products from the $j+1^{th}$ volatility bin and the third term

253 in equation (2) represents the loss of precursor from the jth bin. β and γ are assumed to have a value of 1

254 (meaning no fragmentation) but β is zero for the last bin and γ is zero for the first bin.

255

256 Volatility-resolved mass yields for eighteen different organic precursors for C^* bins ranging from 10^{-1} to

257 10^3 µg m^{-3} were adopted or refit based on low and high NO$_X$ parameterizations published in the literature;

258 organic precursors, the high and low NO$_X$ VBS mass yields, and the relevant references are listed in

259 Tables 2 and 3. Since there were no direct low NO$_X$ VBS parameterizations for alkanes, parameterizations

260 for linear, branched, and cyclic alkanes were developed using pseudo chamber data generated with the

261 SOM based on the low NO$_X$ parameters listed in Table 5 for n-dodecane, methylundecane, and

262 hexylcyclohexane respectively. Some of these parameterizations accounted for vapor wall losses and have

263 been accordingly marked in Tables 2 and 3. Each SOA precursor in the exhaust emissions was assigned a

264 surrogate from Table 2/3 to model SOA formation in the VBS model. When using the high NO$_X$

265 parameterizations, branched and cyclic alkanes were assigned surrogates based on equivalent linear

266 alkanes, following the work of Lim and Ziemann (2009) and Tkacik et al. (2012). A C_X branched alkane

267 was assigned a C_{X-2} linear alkane as a surrogate and a C_X cyclic alkane was assigned a C_{X+2} linear alkane

268 as a surrogate. Since we only fit alkanes up to *n*-heptadecane, we considered *n*-heptadecane as a surrogate

269 for alkanes C_{17}-C_{22}. The Idle-Diesel-None and Idle-Biodiesel-None experiments used the low NO_X

270 parameterizations while all the other experiments used the high NO_X parameterizations. The mass transfer

271 (condensation/evaporation) of the VBS products to the particle phase was assumed to be kinetically-

272 limited in the OFR (Palm et al., 2016;Jathar et al., 2017a;Ahlberg et al., 2017); Section 2.3 describes the

273 mass transfer equation used to model kinetic gas/particle partitioning.

274

275 **2.2.2 Statistical Oxidation Model**

276 The Statistical Oxidation Model (SOM), developed by Cappa and Wilson (2012) is a semi-explicit,

277 parameterizable model that allows for a statistical representation of the coupled chemistry,

278 thermodynamic properties, and gas/particle partitioning of OA. The SOM uses a 2-dimensional carbon-

279 oxygen grid to track gas- and particle-phase precursors and products from precursor oxidation. Each cell

280 in the SOM grid represents a model organic species with a molecular weight defined by the formula

281 $C_xH_yO_z$. A SOM species reflects the average properties (e.g. C^*, reactivity) of all actual species with the

282 same number of carbon (N_C) and oxygen (N_O) atoms that are produced from a given precursor class (e.g.,

283 benzene, alkanes). In the SOM, all gas-phase species are assumed to be reactive towards OH and the OH

284 reaction rate constant (k_{OH}) is calculated using equation 3 as follows:

285 $$log(k_{OH}) = A_1 + A_2 \times (N_C^{A_3}) \times exp(-1 \times \frac{E_a}{8.314 \times T}) \times [1 + \frac{b_1}{\sigma\sqrt{2\pi}} exp(-\frac{1(ln(N_O+0.01)-ln(b_2))^2}{2\sigma^2})] \quad (3)$$

286 $$\sigma (N_C \leq 15) = 0.0214 \times N_C + 0.5238$$

287 $$\sigma (N_C \geq 15) = -0.115 \times N_C + 2.695$$

288 $$b_1 = -0.2583 \times N_C + 5.8944$$

289 $$b_2 (N_C \leq 15) = 0.0314 \times N_C + 0.9871; \quad b_2 (N_C > 15) = 0.25 \times N_C - 2.183$$

290 where A_1=15.1, A_2=3.94, and A_3=0.797. k_{OH} for a specified N_C and N_O is assumed to be the same for

291 species in all the SOM grids.

292

293 The reactions with OH lead to either functionalization or fragmentation, resulting in movement through

294 the carbon-oxygen grid. Six precursor-specific adjustable parameters are assigned for each SOM grid:

295 four parameters that define the molar yields of the four functionalized, oxidized products ($p_{O,k}$, $\Sigma p_{O,k}$=1

296 and hence one out of the four parameters is determined by mass balance), one parameter that determines

297 the probability of functionalization or fragmentation (P_{Frag}, $P_{Func}=1-P_{Frag}$) and one parameter that

298 describes the change in C^* associated with the addition of one oxygen atom (ΔLVP). Equation 4

299 represents the evolution of species in the SOM grid:

300 $$\frac{d[C_X O_Z]}{dt} = -k_{OH}^{X,Z}[OH][C_X O_Z] + [OH]\sum_{k=1}^{4} k_{OH}^{X,Z-k} P_{func}^{X,Z-k} p_{O,k}[C_X O_{Z-k}] +$$

301 $$[OH]\sum_{j=1}^{j_{max}}\sum_{k=0}^{k_{max}-Z} k_{OH}^{X+j,Z-1+k} \frac{P_{frag}^{X,Z-1+k}}{N_{fragments}^{X,Z}}[C_X O_{Z-1+k}] \qquad (4)$$

302 where $C_X O_Z$ is the gas + particle-phase concentration of the SOM species with X carbon atoms and Z

303 oxygen atoms (μg m^{-3}) and $N_{fragments}$ is the number of possible products from fragmentation. The

304 probability of fragmentation is modeled using equation 5 as a function of the O:C ratio because higher

305 O:C ratio compounds are expected to have a higher probability of fragmentation (Chacon-Madrid and

306 Donahue, 2011):

307 $$P_{frag} = \left(\frac{N_O}{N_C}\right)^{m_{frag}} \qquad (5)$$

308 The C^* for each SOM species was calculated using equation 6 as follows:

309 $$log_{10} C^* = -0.337 MW_{HC} + 11.56 - (N_O \times \Delta LVP) \qquad (6)$$

310 where MW_{HC} (g mole^{-1}) is the molecular weight of the hydrocarbon backbone (accounting only for the

311 carbon and hydrogen atoms).

312

313 The parameters used to model SOA formation were based on those published in Cappa et al. (2016) and

314 are listed in Tables 4 and 5. These parameter sets were developed by fitting the SOM predictions to

315 chamber measurements of SOA mass concentrationsand include corrections to account for vapor wall

316 losses (Zhang et al., 2014). Each SOA precursor in the exhaust emissions was assigned a surrogate from

317 Table 4 or 5 to account for the oxidation chemistry associated with oxidation of that species. For example,

318 pentadecane used the parameterization developed by fitting n-dodecane. The difference in the initial

319 number of carbons and oxygens, and thus the volatility, between the surrogate compound and the

320 precursor compound of interest was accounted for, with consequent impact on the SOA yield. In other

321 words, unlike the VBS where the SOA mass yield of the SOA precursor and surrogate is identical, the

322 surrogate in the SOM only informed the statistical trajectory for multi-generational oxidation of a given

323 precursor, and the surrogate and actual compound of interest can have different SOA mass yields. The

324 Idle-Diesel-None and Idle-Biodiesel-None experiments used the low NO$_X$ parameters while all the other

325 experiments used the high NO$_X$ parameters. Similar to the VBS model, the mass transfer

326 (condensation/evaporation) of the SOM products to the particle phase was assumed to be kinetically-

327 limited in the OFR (Palm et al., 2016;Jathar et al., 2017a;Ahlberg et al., 2017) and Section 2.3 below

328   describes the mass transfer equation used to model kinetic gas/particle partitioning.

329

330   **2.3 Kinetic Gas/Particle Partitioning**

331   Palm et al. (2016), (Ahlberg et al., 2017), and Jathar et al. (2017a) have argued that the short residence

332   times and small condensation sinks in the OFR may not permit all low-volatility products formed from

333   precursor oxidation to condense onto preexisting aerosol. Hence, unlike earlier work that has assumed

334   equilibrium partitioning to model SOA in OFRs (Tkacik et al., 2014;Chen et al., 2013), we modeled the

335   kinetic gas/particle partitioning of OA using equation 7 (Zhang et al., 2014):

336   $$\frac{dC_i^p}{dt} = 2\pi D_i D_p N_p F_{FS}\left(C_i^g - \frac{C_i^p C_i^*}{C_{OA}}\right) \tag{7}$$

337   where C_i^p is the particle-phase mass concentration for the ith organic species ($\mu g\ m^{-3}$), D_i is the gas-phase

338   diffusion coefficient of the ith organic species ($m^2\ s^{-1}$), D_p is the number mean particle diameter (m) , N_p is

339   the total particle number concentration (m^{-3}), F_{FS} is Fuchs-Sutugin correction for non-continuum mass

340   transfer, C_i^g is the gas-phase mass concentration of the ith organic species ($\mu g\ m^{-3}$), C_i^* is the effective

341   saturation concentration of the ith organic species, and C_{OA} is the total OA mass concentration ($\mu g\ m^{-3}$).

342   The ith organic species refers to the organic compounds tracked in the VBS bins and the SOM grids. The

343   gas-phase diffusion coefficient was calculated for each organic species as follows:

344   $$D_i = D_{CO_2}\frac{MW_{CO_2}}{MW_i} \tag{8}$$

345   where D_{CO_2} is the gas-phase diffusion coefficient of CO_2 ($1.38\times10^{-5}\ m^2\ s^{-1}$), MW_{CO_2} ($g\ mole^{-1}$) is the

346   molecular weight of CO_2, and MW_i ($g\ mole^{-1}$) is the molecular weight of the ith organic species. In the

347   VBS model where we do not track the molecular composition of the SOA species, we assumed all

348   condensing species to have a molecular weight of 200 $g\ mole^{-1}$. This formulation to calculate the gas-

349   phase diffusion coefficient under-predicted the measured gas-phase diffusion coefficients compiled by

350   Tang et al. (2015) by ~20%. However, doubling the gas-phase diffusion coefficient calculated in equation

351   8 resulted in very small change (<1%) in the OA mass predictions for a representative experiment. Hence,

352   we decided to use the formulation in equation (8) for the rest of this work. The Fuchs-Sutugin correction

353   was calculated as follows:

354   $$F_{FS} = \frac{0.75\alpha(1+Kn)}{Kn^2+Kn+0.283\cdot Kn\cdot\alpha\ +0.75\alpha} \tag{9}$$

355   $$Kn = \frac{2\lambda_i}{D_p} \tag{10}$$

356   $$\lambda_i = \frac{3D_i}{C_j} \tag{11}$$

357 $$C_i = \sqrt{\frac{8N_A kT}{\pi MW_i}} \qquad\qquad\qquad\qquad (12)$$

358   where Kn is the Knudsen number, α is the mass accommodation coefficient, λ_i is the mean free path of the

359   i^{th} organic species in air (m), C_i is the root mean square speed of the gas (m s^{-1}), N_A is Avogadro's number

360   (molecules mole^{-1}), k is the Boltzmann constant (m^2 kg s^{-2} K^{-1}), and T is the temperature (K).

361

362   **2.4 Model Inputs**

363   **2.4.1 Semi-Volatile and Reactive POA**

364   Previous work has shown that much of combustion-related POA is semi-volatile and exists in an

365   equilibrium with gas-phase vapors (Robinson et al., 2007;Huffman et al., 2009;May et al., 2013c, b;May

366   et al., 2013a). Jathar et al. (2017a) measured emissions of POA at no OH exposure and these measured

367   concentrations were used to initialize the seed OA available for partitioning in the OFR and to calculate

368   the mass concentrations of vapors in equilibrium with the POA. The mass concentrations of the POA

369   vapors were determined based on the normalized, volatility-resolved distribution of primary organic

370   compounds estimated by May et al. (2013b) for emissions from a suite of on- and off-road diesel vehicles.

371   The volatility distribution of May et al. (2013b) for diesel primary organic compounds is listed in Table

372   6(a). For the SOM, we assumed that the primary organic compounds could be represented using a

373   distribution of n-alkanes and we refit the volatility distribution in Table 6(a) to develop a carbon-number

374   resolved distribution of n-alkanes; this distribution is listed in Table 6(b).

375

376   **2.4.2 SOA Precursors**

377   Jathar et al. (2017a) did not speciate the THC or SOA precursor emissions from the diesel engine and

378   hence we have developed our own emissions profiles based on previously published literature to speciate

379   the THC emissions. In this work, we used two different emissions profiles listed in EPA SPECIATE

380   version 4.3 that are commonly used to speciate THC emissions from diesel engines for emissions

381   inventories used in atmospheric modeling (EPA, 2013): Profiles #3161 (Diesel Exhaust- Farm

382   Equipment) and #8774 (Heavy Duty Diesel Exhaust). Profile #3161 best matched the diesel engine source

383   and diesel fuel used by Jathar et al. (2017a) and was used as the baseline emissions profile to speciate the

384   THC emissions; we examined the sensitivity of using Profile #8774 on model predictions. We were

385   unable to find a comprehensive emissions profile for THC emissions from the use of straight biodiesel

386   fuel in the literature, and have relied on emissions profiles that were determined for biodiesel-diesel

387   blends. Profile #4777 (30% Biodiesel Exhaust - Light Duty) was used as the baseline emissions profile to

388   speciate THC emissions for experiments performed using the biodiesel fuel. All three emissions profiles

389   (3161, 8774, and 4777) are listed in Tables S2 through S4.

390

391   Prior work in studying SOA formation has revealed that traditional speciation of THC emissions does not

392   include emissions of high molecular-weight organic compounds, such as IVOCs, that are important SOA

393   precursors (Jathar et al., 2014b). In Profile #3161 such compounds are partially accounted for in the

394   'unknown' species category (13.76% by mass of THC). Zhao et al. (2015) recently estimated that IVOCs

395   were 60% of the THC emissions from a suite of on- and off-road diesel engines and provided a semi-

396   explicit speciation of the IVOC emissions as a carbon-number distribution of linear, branched and cyclic

397   alkanes. To account for these IVOC emissions, we assumed that the base case emissions profiles

398   contained 30% IVOCs on a mass-basis (this IVOC fraction was selected since it resulted in the most

399   optimum model-measurement comparison for OA mass; this will be discussed later in Section 3.3) and

400   had the same chemical speciation as that proposed by Zhao et al. (2015) for an off-road engine

401   (transportation refrigeration unit). We performed sensitivity simulations using IVOC fractions of 0%

402   (assuming that the THC emissions contained no IVOCs), 13.76% (based on the 'unknown' category in

403   Profile #3161), and 60% (based on the median estimate in Zhao et al. (2015)), on a mass-basis. Addition

404   of IVOCs to the emissions profile meant that the VOC species (e.g. benzene, toluene, short alkanes) had

405   to be renormalized to accommodate the IVOCs. Table 7 lists the renormalized baseline emissions profiles

406   for SOA precursors used for diesel and biodiesel exhaust with 30% IVOCs along with the reaction rate

407   constants with OH (k_{OH}) and surrogates (or model compound) used to model SOA formation for the VBS

408   and SOM models. Concentrations for each species were determined by multiplying the experiment-

409   specific THC mass concentrations with the renormalized emissions profiles.

410

411   **2.4.3 Particle Size and Particle Number Concentrations**

412   For numerical simplicity, we used a monodisperse aerosol, the properties of which (number mean

413   diameter (D_p) and number concentration (N_p)) were initialized from the measured particle size distribution

414   data when modeling kinetic gas/particle partitioning. For experiments performed without the DPF+DOC,

415   the initial particle number concentrations and condensational sinks were high (>3.3×10^5 # cm^{-3} and >0.5

416   min^{-1}) and hence the monodisperse aerosol was initialized based on data at no photochemical exposure.

417   For experiments performed with the DPF+DOC where the initial particle number concentrations were

418   relatively low (<1000 # cm^{-3} and <0.003 min^{-1}), photochemical aging resulted in formation and growth of

419   new particles and provided a substantial increase in the surface area (>factor of 300) available for

420   condensation. In these experiments, we initialized the monodisperse aerosol using an average of the data

421   at no photochemical exposure and after photochemical exposure (Palm et al., 2016). Averaging the data

422   allowed for a more realistic estimate of the condensational sink. In each simulation, the condensing SOA

423   mass was used to calculate the change in particle size but the number concentration was conserved. The

424   number mean diameter and the number concentration data - representing the initial condensational sink –

425   for all experiments are listed in Table 1.

426

427   New particle formation and growth was observed for most experiments at or near the highest

428   photochemical ages (at or >1 OH day), which presumably influenced the condensational sink at the

429   beginning of the experiment. Therefore, we performed sensitivity simulations to investigate the influence

430   of new particle formation on model predictions. We performed simulations with each model (VBS and

431   SOM) with four different initial condensational sinks. The first three simulations used measured data to

432   calculate the initial condensational sink inputs: (i) number mean diameter and measured number

433   concentration at no OH exposure (equivalent to the default for non-DPF+DOC experiments), (ii) number

434   mean diameter and measured number concentration at the given OH exposure, and (iii) average of (i) and

435   (ii) (default for DPF+DOC experiments). The fourth simulation (iv) assumed that the OFR nucleated 1

436   nm particles at the beginning of the experiment where the number concentration of these particles was

437   equal to that measured at the end of the experiment.

438

439   **2.5 Model Simulations and Model Code**

440   The VBS and SOM models were run separately for each photochemical exposure simulated for each

441   experiment listed in Table 1. In the VBS simulations, POA was tracked in one basis set while products

442   from each SOA precursor were tracked in separate basis sets, allowing us to distinguish between POA and

443   SOA. In the SOM simulations, all precursor molecules with the same surrogate (e.g., all *n*-alkanes) were

444   tracked in the same SOM grid. Model simulations were performed in phases to answer specific questions

445   and inform model inputs for later simulations:

446   1. To provide a general overview of the model predictions and model-measurement comparison, and

447   to orient the reader to the results thereafter, we performed simulations with the VBS and SOM

448   models using the base set of inputs for one of the Idle-Diesel-None experiments. Our base case

449   included: Profile #3161 for VOC emissions, 30% IVOC mass fraction, kinetic gas/particle

450   partitioning with a mass accommodation coefficient of 0.1, and monodisperse aerosol inputs based

451   on measured data at no photochemical exposure. The partitioning- and IVOC-related choices for

452   the base case are discussed in Sections 3.2 and 3.3 respectively.

453   2. Models used to simulate SOA production in environmental chambers and OFRs have typically

454   assumed instantaneous equilibrium partitioning (e.g., Chen et al. (2013)). To examine the validity

455   of assuming instantaneous equilibrium partitioning, we performed simulations with the VBS and

456   SOM models using instantaneous or kinetic gas/particle partitioning for one of the Idle-Diesel-

457   None and the Idle-Diesel-DPF+DOC experiments. Kinetic partitioning was modeled using three

458   values of the mass accommodation coefficient (α=0.01, 0.1, 1) to capture the uncertainty in its true

459   value. To examine the influence of an increased initial condensational sink from new particle

460   formation on kinetic partitioning, we performed additional simulations using four different initial

461   condensational sinks (see Section 2.4.3) on one of the Idle-Diesel-None and the Idle-Diesel-

462   DPF+DOC experiments.

3. Previous work has shown that combustion-related IVOCs are important precursors of SOA (e.g.,
    Jathar et al. (2014b)). To investigate the importance of IVOCs, we performed simulations with the
    VBS and SOM models at four different assumed IVOC mass fractions (0%, 13.76%, 30%, and
    60%), as discussed above when discussing the THC profiles, at all photochemical exposures and
    for all the experiments listed in Table 1. We performed additional simulations with different
    emissions profiles and SOA parameterizations on one of the Idle-Diesel-None experiments to
    investigate uncertainties linked to the composition and SOA potential of IVOCs.

4. Additional simulations were performed to examine the sensitivity of model predictions to the
    following processes: multi-generational aging, vapor wall losses, residence time distributions, and
    spatial heterogeneity in OH concentrations.

473   The numerical codes for the VBS were developed in Matlab while those for the SOM were developed in

474   IGOR (WaveMetrics Inc.). These codes will be made available on request. The simulations were

475   performed on an Intel i5 processor (1.7 GHz) and required ~10 s to perform a VBS simulation and ~500 s

476   to perform a SOM simulation at a single photochemical exposure.

477

3. Results

3.1 General Model Results Using the Base Case

480   In Figure 1, we compare predictions of OA from the VBS and SOM models using the base case to the

481   measurements for the Idle-Diesel-None experiment performed on June 5. Figures 1(a) and 1(b) compare

482   predictions to the measurements in units of $\mu g\ m^{-3}$ and g kg-fuel^{-1}, respectively; hereafter we present all

483   mass predictions in units of g kg-fuel^{-1}. For this experiment, the VBS/SOM models over-predicted the OA

484   mass by a factor of 1.9/2.2 at the lowest photochemical exposure (0.06 OH days) and a factor of 1.6/1.8 at

485   the next highest photochemical exposure (0.17 OH days). The over-prediction was because the models

486   significantly over-predicted the SOA formation at these two photochemical exposures. For higher

487   photochemical exposures (>0.5 OH days), both models slightly under-predicted the OA mass but

488 predictions were still within the measurement uncertainty. Our base case seemed to offer a mixed model-

489 measurement comparison for this specific experiment (i.e., over-prediction at lower photochemical ages

490 and a slight under-prediction at higher photochemical ages) because the 30% IVOC mass fraction used in

491 the base case was optimized to achieve a favorable model-measurement comparison across all

492 experiments at all photochemical exposures. In other words, the over-prediction in this experiment at

493 lower photochemical exposures was probably offset by an under-prediction at similar photochemical

494 exposures for some of the other experiments. It is important to note that the model performance varied

495 across the suite of experiments and this overall model performance is discussed in more detail in Section

496 3.3. The VBS and SOM models predicted that the OA at the maximum photochemical exposure was

497 dominated by SOA produced from VOC and IVOC oxidation (92-93%), which agreed well with the

498 measured composition (see Figure 1(c)). For the measurements, POA was defined as fresh OA while SOA

499 was defined as OA formed in addition to the POA. Furthermore, both models suggested that most of the

500 SOA emanated from the oxidation of IVOCs with only 7-14% resulting from the oxidation of aromatic

501 VOCs and less than 0.6-4% resulting from alkane VOCs smaller than a C_{12}. This dominance of IVOCs in

502 explaining the photochemically produced SOA is in line with previous OFR and chamber studies that

503 have modeled SOA formation from diesel exhaust (Tkacik et al., 2014;Zhao et al., 2015;Jathar et al.,

504 2014b).

505

506 **3.2 Kinetic Gas/Particle Partitioning**

507 In Figure 2, we plot predictions from the VBS and SOM models for the Idle-Diesel-None and Idle-Diesel-

508 DPF+DOC experiments assuming instantaneous and kinetic gas/particle partitioning. The two different

509 experiments were deliberately chosen to highlight the role instantaneous partitioning plays at the

510 extremities. We found that for the Idle-Diesel-None experiment, the use of instantaneous partitioning

511 roughly produced the same result as kinetic partitioning with α values of 0.1 and 1 and that all these

512 predictions resulted in roughly the same model-measurement comparison. The instantaneous partitioning

513 predictions were slightly higher than the kinetic partitioning predictions for the VBS simulations. The

514 kinetic partitioning simulations (except for that with an α of 0.01) produced the same result as the

515 instantaneous partitioning simulation most likely because the initial condensational sink was large enough

516 (1.12 min^{-1}) in this experiment that there were no kinetic limitations to partitioning. The increase in the

517 condensational sink through condensation of SOA (10 min^{-1} at the highest photochemical exposure)

518 tended to further reduce any differences in the predictions between the kinetic and instantaneous

519 partitioning simulations. However, for the Idle-Diesel-DPF+DOC experiment, the instantaneous

520 partitioning simulation predicted substantial OA mass at the lower photochemical exposures (0.04 and

521   0.12 OH days) compared to the kinetic partitioning simulations, specifically a factor of 9.8-29 larger at

522   0.04 OH days and a factor of 9.7-75 larger at 0.12 OH days for the VBS model and a factor of 3.9-5.8

523   larger at 0.04 OH days and a factor of 6.4-9.1 larger for the SOM. The instantaneous partitioning

524   simulations predicted a lot more SOA because all condensable products of organic precursor oxidation

525   were allowed to condense instantaneously (according to their respective volatilities) while the kinetic

526   partitioning simulations predicted little SOA production because the initial condensational sink was quite

527   small (0.002 min^{-1}). Predictions from the instantaneous and kinetic partitioning simulations were much

528   closer at the higher photochemical exposures because the SOA formed had grown the condensational sink

529   enough to reduce limitations to partitioning (1 min^{-1} at the highest photochemical exposure). These results

530   imply that the condensation of SOA in OFRs, in some instances, could be kinetically-limited and that

531   instantaneous partitioning may result in models over-predicting the condensation and formation of SOA.

532

533   We make two additional observations based on the results in Figure 2. First, the initial condensational

534   sink for the Idle-Diesel-None experiment was large (1.12 min^{-1}) compared to condensational sinks one

535   would encounter in the real atmosphere. For example, 5 μg m^{-3} of aerosol in a representative rural or

536   remote environment will have a condensational sink <0.05 min^{-1} (Seinfeld and Pandis, 2006). Therefore,

537   modeling ambient applications of the OFR or OFR use with sources that use emissions control devices

538   will need to be even more mindful of the instantaneous partitioning assumption while predicting SOA

539   formation. Second, for the kinetic partitioning results, predictions from both models were relatively less

540   sensitive to α values between 0.1 and 1 but were dramatically lower for an α value of 0.01; more than a

541   factor of 2 for the Idle-Diesel-None experiment and more than an order of magnitude for the Idle-Diesel-

542   DPF+DOC experiment. Given the low sensitivity to α values greater than 0.1 and the reasonable model-

543   measurement comparison at an α value of 0.1 and 1 at least for the Idle-Diesel-None experiment, we

544   argue that the SOA condensation can be represented by an α value larger than 0.1 for the OFR

545   experiments in this work. This α value for diesel exhaust SOA was consistent with prior estimates of the α

546   value for biogenic SOA estimated from chamber, OFR, and aerosol heating experiments (Lee et al.,

547   2011;Saleh et al., 2013;Karnezi et al., 2014;Palm et al., 2016) and direct measurements of α for alkanol

548   SOA (Krechmer et al., 2017). However, an α of 0.1 was an order of magnitude higher than that observed

549   recently for toluene SOA under dry conditions (Zhang et al., 2014). Model results presented hereafter

550   include a kinetic treatment of gas/particle partitioning and assumed an accommodation coefficient of 0.1.

551

552   Results from model simulations performed using different initial condensational sink inputs, some of

553   which captured the influence of new particle formation, are plotted in Figure 3. We found that the initial

554   condensational sink had no influence on the OA predictions from both models for the Idle-Diesel-None

555   experiment, despite substantial differences in the initial condensational sink between the different cases.

556   This was because the amount of SOA formed (920 μg m^{-3} at the highest photochemical exposure) was

557   sufficient to grow the condensational sink enough that the initial condensational sink did not matter. In

558   contrast, for both models we found large differences between the model predictions of OA for the Idle-

559   Diesel-DPF+DOC experiment. The use of inputs based on the measurements at no OH exposure, where

560   the aftertreatment system significantly reduced number concentrations (910 cm^{-3}) and hence the available

561   condensational sink (0.002 min^{-1}), produced much less SOA (an order of magnitude lower or more) and

562   poorer agreement with the measurements (see curve (i) in Figure 3(b)). Initial condensational sinks that

563   captured the influence of new particle formation resulted in higher model predictions but were still about

564   a factor of ~2 lower for the VBS simulations and a factor of ~2.7 lower for the SOM simulations when

565   compared against the measurements. The DPF+DOC results also suggest that calculating an initial

566   condensational sink using data from before and after the photochemical exposure, as done by Palm et al.

567   (2016), could be used as an input to model OFR data. Slight differences between the different curves for

568   the Idle-Diesel-None experiment and curves (ii), (iii), and (iv) for the Idle-Diesel-DPF+DOC experiment

569   can be attributed to the interaction of multigenerational aging and kinetic gas/particle partitioning.

570

571   **3.3 Influence of IVOCs on SOA Formation**

572   In Figure 4(a), we compare predictions of SOA concentrations from the SOM against measurements for

573   all the experiments listed in Table 1 and at all photochemical exposures. For visual clarity, we do not

574   present results from the VBS model as both models had nearly identical predictions with a few

575   exceptions; see Figure S1 where we compare VBS model predictions to SOM predictions for all

576   experiments at all photochemical exposures for the base case. The four panels in Figure 4(a) show model-

577   measurement comparisons assuming four different fractions of IVOCs: 0%, 13.76%, 30%, and 60%;

578   statistical metrics of fractional bias, fractional error, and R^2 for the comparison for both models are listed

579   in Table S4 (fractional bias $= \frac{1}{N}\sum_{i=1}^{n}\frac{M-O}{\frac{M+O}{2}}$, fractional error $= \frac{1}{N}\sum_{i=1}^{n}\frac{|M-O|}{\frac{M+O}{2}}$, M=predicted value,

580   O=observed value, N=sample size). The model-measurement comparison and the model skill was very

581   poor when no IVOCs were included (fractional bias = -109%, fractional error = 125%, and $R^2 = 0.52$);

582   this model reflects the treatment of diesel-powered sources in most traditional emissions inventories and

583   large-scale models. The model-measurement comparison was reasonable with 13.76% IVOCs (fractional

584   bias = -46%, fractional error = 101%, and $R^2 = 0.95$) but model predictions were over-predicted with 60%

585   IVOCs (fractional bias = 72%, fractional error = 97%, and $R^2 = 0.99$). The optimal model performance

586 that produced the lowest fractional bias and fractional error was realized at an IVOC mass fraction of 30%

587 (fractional bias= 6%, fractional error= 86%, and R^2 = 0.88). For predictions with an IVOC mass fraction

588 of 30%, 66% and 70% of the model predictions were within a factor of 1.5 and 2 of the measurements and

589 IVOCs on average accounted for 67%/72% (VBS/SOM) of the SOA at the highest photochemical

590 exposure across all experiments. Given the optimal performance, the base case used in this work assumed

591 a 30% IVOC fraction. These comparisons indicate that it is critical that IVOCs be included when

592 modeling the SOA formation from diesel exhaust and also validate the IVOC composition estimates made

593 by Zhao et al. (2015).

594

595 We further investigated the IVOC species that contributed the most to SOA formation. For an IVOC

596 fraction of 30%, cyclic alkane IVOCs accounted for 23% of the THC emissions and on average accounted

597 for 61%/53% (VBS/SOM) of the SOA formation across the different experiments. We should note that

598 the speciation of cyclic alkane IVOCs in Zhao et al. (2015), while robust in quantifying the carbon

599 number, did not include any specificity in terms of the molecular structure, i.e., their methods would not

600 be able to distinguish between a pure C_{10} cyclic alkane and a cyclohexane with a 4-carbon branch.

601 Further, the parameterizations to model SOA formation from cyclic alkane IVOCs for both models were

602 based on the behavior of particular compounds. In the VBS model when using the high NO_X

603 parameterizations, the surrogate for a cyclic alkane IVOC was determined through equivalence with a

604 straight alkane IVOC while in the VBS model when using the low NO_X parameterizations or the SOM the

605 cyclic alkane IVOCs were tied to parameterizations for hexylcyclohexane. (The observed SOA yield and

606 derived SOM parameterization for hexylcyclohexane is actually quite similar to that for cyclododecane

607 for low-NO_X conditions, but not for high-NO_X conditions (Cappa et al., 2013)) This lack of specificity in

608 the speciation and the SOA parameterizations made the SOA predictions from the oxidation of cyclic

609 alkane IVOCs relatively uncertain. To examine the sensitivity of the model predictions to uncertainties in

610 the model treatment of cyclic alkane IVOCs, we performed simulations with both models for one of the

611 Idle-Diesel-None experiments where the cyclic alkane IVOCs were treated as branched alkane IVOCs;

612 results from these simulations are shown in Figure 5(a). The use of branched alkane IVOCs to model

613 cyclic alkane IVOCs only marginally reduced OA predictions for both the VBS and SOM models,

614 suggesting that the model predictions were not sensitive to the SOA parameterization used for cyclic

615 alkane IVOCs. Regardless, we recommend that future work focus on a more detailed speciation of cyclic

616 alkane IVOCs in combustion emissions as well as on chamber and OFR experiments on those speciated

617 compounds to improve quantification of their SOA mass yields.

618

619   As there were no direct measurements of any SOA precursors in the study of Jathar et al. (2017a), we

620   have used previously published emissions profiles for diesel exhaust to determine initial concentrations of

621   the SOA precursors. We examined the sensitivity of model predictions to two different emissions profiles

622   from the EPA SPECIATE (version 4.3) database: Profile #3161 (included in the base case) and Profile

623   #8774 that represents emissions from 'Heavy Duty Diesel Exhaust'; the speciation for both profiles is

624   provided in Tables S2 and S3. Both profiles only included speciation for VOC emissions and in these

625   simulations we assumed an IVOC mass fraction of 30%. The results captured in Figure 5(b) for one of the

626   Idle-Diesel-None experiments show that the choice in the emissions profile had no influence on the OA

627   evolution for the VBS model but had a small influence on the OA evolution for the SOM. This little to

628   small influence was expected given that most of the SOA was formed from IVOC, rather than VOC,

629   oxidation. This further demonstrates that IVOCs, not VOCs, play an important role in controlling the

630   SOA formation from diesel exhaust emissions and it is important that future studies work towards better

631   understanding the IVOC speciation.

632

633   The IVOC speciation of Zhao et al. (2015) included 37 unique species, each of which required a unique

634   surrogate to model the SOA formation from that species. Tracking these many IVOC species in an

635   atmospheric model (e.g., global climate model) may be intractable and hence, there is a need to develop

636   simplified parameterizations to efficiently model SOA formation from IVOCs. We note that species using

637   the same surrogate in the VBS model (e.g., a C_{15} linear alkane, C_{17} branched alkane, and C_{13} cyclic alkane

638   are all parameterized using *n*-pentadecane when using the high NO_X parameterizations) could be lumped

639   together to reduce the number of precursors and products tracked and that there are no penalties for a

640   precursor type (e.g., *n*-alkanes) to include additional precursor and product species once a SOM grid is

641   setup. Nonetheless, to investigate the possibility of developing a simplified parameterization, we modeled

642   SOA from IVOCs assuming that all the IVOCs could be modeled together as a single linear C_{13}, C_{15}, C_{17}

643   or C_{19} alkane; a similar strategy was employed by (Jathar et al., 2014b) to model SOA formation from

644   unspeciated organic compounds in combustion emissions. Results from these simulations are shown in

645   Figure 5(c) for one of the Idle-Diesel-None experiments. For the VBS model, the use of a larger carbon

646   number alkane to model IVOC SOA produced increasingly more OA, with the C_{19} alkane providing the

647   best comparison against measurements. For the SOM, the use of a C_{13} and C_{15} alkane produced good

648   agreement with measurements with a C_{13} alkane slightly under-predicting the OA at 0.5 OH days and the

649   C_{15} alkane slightly over-predicting the OA at lower photochemical exposures (0.06 and 0.17 OH days). It

650   was interesting to observe that for the SOM, in contrast to the VBS, the use of different linear alkanes

651   produced different OA masses at lower photochemical exposures but converged at the highest

652   photochemical exposure suggesting that the effective SOA mass yield in the SOM varied dynamically

653   with photochemical age. Differences in the VBS and SOM predictions with different alkane

654   parameterizations point to inherent differences in the coupled representation of multigenerational aging

655   and gas/particle partitioning. Results from these simulations indicate that in cases where computational

656   efficiency is demanded, the SOA formation from IVOCs in diesel exhaust could be modeled using a

657   surrogate linear alkane, possibly a C_{19} linear alkane with the VBS and a C_{13} or C_{15} linear alkane for the

658   SOM.

659

660   **3.4 Elemental Composition**

661   The SOM tracks both the carbon and oxygen number of the oxidation products, which allowed us to

662   predict the O:C ratio of the OA. The O:C of the OA was calculated by combining the measured O:C of

663   the POA with the modeled O:C of the SOA. We compare predictions of the O:C of OA from the SOM

664   against measurements for all the experiments listed in Table 1 and at all photochemical exposures in

665   Figure 4; statistical metrics of fractional bias, fractional error, and R^2 for the comparison are listed in

666   Table S5. Model predictions for the no IVOC case, where the O:C of the OA was dominated by the O:C

667   of the aromatic SOA, compared well with measurements (fractional bias = -4.2%, fractional error = 28%,

668   and $R^2 = 0.77$). However, the poor OA mass predictions with no IVOCs suggests that the good O:C

669   performance was purely coincidental. The 13.76%, 30%, and 60% IVOC cases under-predicted the OA

670   O:C where the under-prediction appeared to increase as the IVOC influence increased; fractional bias = -

671   32%, fractional error = 38%, and $R^2 = 0.72$ for the 13.76% IVOC case, fractional bias = --37%, fractional

672   error = 42%, and $R^2 = 0.70$ for the 30% IVOC case, and fractional bias = -60%, fractional error = -62%,

673   and $R^2 = 0.46$ for the 60% IVOC case. A higher IVOC fraction resulted in a lower O:C ratio because the

674   IVOCs were primarily composed of higher carbon number species that on oxidation produced low O:C

675   SOA compared to SOA formed from precursors such as aromatics. On average, the 30% IVOC case

676   predicted an O:C ratio that was 28% lower than the measurements. For the three non-zero IVOC cases

677   (13.76%, 30%, and 60%), the model skill in predicting the O:C was much better for the non-DPF+DOC

678   experiments ($R^2 = 0.82$, 0.83, and 0.80 respectively) than for the DPF+DOC experiments ($R^2 = 0.02$, 0.02,

679   and 0.29 respectively). Measurements and model predictions of the OA O:C ratio from the 30% IVOC

680   case as a function of photochemical age are presented in Figure S2.

681

682   The under-prediction in O:C ratios was confounding when compared to earlier applications of the SOM

683   and in light of the reasonable model-measurement comparison found in this work in predicting OA mass.

684   We note that the low O:C in the 13.76%, 30%, and 60% IVOC cases stems from the dominance of

685   product species that have high carbon numbers and low oxygen numbers. We explored several lines of

686   reasoning for this under-prediction. First, Cappa et al. (2013) found good agreement between the SOM-

687   predicted and observed O:C for chamber experiments conducted using individual linear, branched and

688   cyclic C_{12} alkanes. Also, general predictions of the dependence of O:C on the carbon number of the parent

689   hydrocarbon (cf. Fig. 2b in Cappa and Wilson (2012)) show good agreement with observations (cf. Fig.

690   2a in Tkacik et al. (2012)), both in terms of absolute values and shape. This suggests that uncertainties in

691   the SOM parameters may not be the dominant reason for the under-prediction. A possible reason for the

692   under-prediction then is that the compounds identified by Zhao et al. (2015) as IVOCs are structurally

693   different than the alkanes used to model them in this work. Second, the gas-phase chemistry in the OFR

694   might be inherently different than that in a chamber. For example, kinetic limitations to gas/particle

695   partitioning may result in gas-phase oxidation of low-volatility products having high O:C that typically

696   would have partitioned to the particle phase in a chamber experiment but instead are fragmented (Palm et

697   al., 2016). As to why the chamber-based SOM parameters then offer good model performance on OA

698   mass remains unclear. One way in which this issue could be addressed in the future is by developing

699   SOM parameters exclusively based on OFR data, as and when they become available. Third, the SOM

700   used here did not include surface/heterogeneous and particle-phase reactions that might influence the OA

701   composition and O:C ratio. When heterogeneous reactions of OA were included assuming an OH uptake

702   coefficient of 1 (the product distribution from the oxidation reaction was kept the same as the gas-phase

703   reactions), SOA production at the highest photochemical exposure for all the experiments was reduced, on

704   average, by 7% from fragmentation reactions within the particle phase, but the O:C ratio was only

705   marginally increased (average of 2%).

706

707   To understand the O:C under-prediction better, we compared model predictions of normalized gas-phase

708   species concentrations from the SOM to normalized gas-phase measurements made by Friedman et al.

709   (2017) using a chemical ionization mass spectrometer (CIMS). The CIMS detects an array of oxygenated

710   organic species and the high resolution of the time-of-flight mass spectrometer enables identification of

711   the elemental composition of each detected peak. The CIMS data were aggregated by carbon and oxygen

712   number to facilitate comparison with the SOM data. The comparison was performed on a normalized

713   basis because the CIMS did not provide absolute concentrations for every detected peak. The SOM-CIMS

714   comparisons for the Idle-Diesel-None and Load-Diesel-None experiments at the highest photochemical

715   exposure are shown in Figure 6, which highlight four findings of note. First, the CIMS measured species

716   larger than a carbon number of 12 that are presumably products from oxidation of higher molecular

717   weight organic compounds, although the possibility of dimer formation in the instrument cannot be

718   entirely ruled out. Nonetheless, this provides additional evidence for the presence of IVOC oxidation

719   products in diesel exhaust emissions. Second, the CIMS measured organic compounds with high O:C

720   ratios (e.g., C_6O_6, C_7O_7). This implies that the reaction chemistry in OFRs rapidly adds functional groups

721   to the carbon backbone, although larger, less oxidized compounds could be simultaneously functionalized

722   and fragmented in the CIMS leading to the appearance of highly oxidized species. Third, the SOM offered

723   a reasonable correlation against the CIMS measurements for both experiments across a majority of the

724   carbon-oxygen combinations that spanned more than four orders of magnitude. Qualitatively, this finding

725   validates the statistical evolution of organic compounds tracked through the generalized SOM

726   mechanism, although certainly some differences are evident. Finally, for the mid-carbon number species

727   ($\sim C_{10}$), the SOM seemed to produce higher fractions of species with low oxygen numbers (O_0 to O_3) but

728   lower fractions of species with high oxygen numbers (O_5 to O_7). This under-prediction of the high oxygen

729   number species might potentially explain why the SOM may be under-predicting the OA O:C ratio. The

730   SOM-CIMS comparison is preliminary and we intend to explore the implications of this comparison in

731   future work.

732

733   **3.5 Other Model Sensitivities**

734   We performed sensitivity analyses to examine the influence of other key processes on predictions from

735   both the VBS and SOM models. When examining the sensitivity to each process, all the other inputs were

736   kept the same as those listed in the base case. We only present sensitivity results for the Idle-Diesel-None

737   experiment performed on June 5, as the results for this experiment were generally representative of all

738   experiments (Figure 7). For completeness, we performed simulations for all the experiments at the highest

739   photochemical exposure since each of the processes explored below manifested the strongest response at

740   the highest photochemical exposure. The results from these simulations are presented as a change in the

741   model predictions relative to that offered by the base case.

742

743   ***Multi-generational Aging.*** One of the key differences between the VBS and the SOM models is how they

744   represent the multi-generational aging of gas-phase products. SOA parameters for the VBS model

745   represent stable product distributions at the end of the chamber experiments and therefore already include

746   the influence of multi-generational aging reactions encountered during the chamber experiment.

747   Additional multi-generational aging in the VBS model, based on the scheme of Robinson et al. (2007), is

748   simulated as a continuous decrease in product volatility, which does not account for fragmentation

749   reactions and has not been constrained against experiments. The SOM framework explicitly models multi-

750   generational aging that includes treatment of fragmentation reactions and constrains the aging reactions

751   based on the chamber experiments to an extent that is determined by the length (in OH exposure space) of

752   the experiment. To test the influence of multi-generational aging, we performed model simulations with

753   aging turned off for the VBS and SOM models and plot the results in Figure 7(a). We found that aging

754   had a small influence (~18% reduction in OA mass) on model predictions from the VBS model, most

755   likely because the high SOA and OA mass concentrations resulted in a substantial fraction of the organic

756   species to be partitioned to the particle phase. This left very little of the organic species in the gas-phase to

757   participate in multi-generational aging. We calculated that less than 20% by mass of the product species

758   in this experiment was in the gas-phase at the OA mass concentration at the highest photochemical

759   exposure, implying that the SOA mass yields at these OA mass concentrations were rapidly approaching

760   100%. In contrast, the absence of aging resulted in a 43% decrease in the OA mass for the SOM. The

761   decrease was mainly because the first generation oxidation product with the highest yield (i.e., C_xO_1) was

762   too volatile to partition to the particle phase and needed to be aged further to form condensable products.

763   As noted earlier, the term aging is defined differently for the VBS and SOM models and the results

764   presented here need to take the definitional issues into account when examining the influence of aging.

765   Compared to the base case, no aging resulted in an average decrease of 4% and 30% in OA mass for the

766   VBS and SOM models respectively for all experiments at the highest photochemical exposure. These

767   simulations suggest that aging of the oxidation products, at least for the SOM, is as important as the

768   contribution of first generation products to SOA formation.

769

770   *Vapor Wall Losses.* Prior work has highlighted the influence vapor wall losses exert on the calculation of

771   SOA mass yields from chamber experiments (Zhang et al., 2014;Krechmer et al., 2016). Cappa et al.

772   (2016), based on the chamber work of Zhang et al. (2014), recently published parameter sets for the SOM

773   that accounted for no vapor wall losses and two different vapor wall loss rates (1×10^{-4} and 2.5×10^{-4} s^{-1})

774   assuming an equivalent OA mass of the chamber walls of 10 mg m^{-3} (the base case used the parameter

775   sets for a vapor wall loss rate of 2.5×10^{-4} s^{-1}). We performed model simulations with SOM using

776   parameters that were either not corrected for vapor wall losses or that were corrected for vapor wall losses

777   using either the low (1×10^{-4}) or high (2.5×10^{-4}) estimates proposed by Cappa et al. (2016). The results

778   plotted in Figure 7(b) show that correcting for vapor wall losses significantly increased model predicted

779   OA mass (by 73% and 112% for the low wall loss and high wall loss cases respectively at the highest

780   photochemical exposure when compared to the no wall loss case) and provided the best performance for

781   the high estimate for vapor wall losses. Across all experiments and at the highest photochemical exposure,

782   accounting for vapor wall losses using the high estimate resulted in an average increase of 39% over no

783   accounting for vapor wall losses. These comparisons suggest that it is important to use SOA

784 parameterizations in which vapor wall losses in chambers have been accounted for when interpreting

785 SOA experiments. Furthermore, we also simulated the influence of vapor losses to the OFR walls on

786 model predictions. We assumed reversible uptake of vapors to the walls and used a vapor wall loss rate of

787 2.5×10^{-3} s^{-1} (factor of ~10 larger than that for a chamber) based on the work of Palm et al. (2016) and an

788 equivalent OA mass concentration of 10 mg m^{-3} for the OFR walls. The results plotted in Figure 7(b)

789 show that the loss of vapors to the OFR walls had a small influence on model predictions: a 6.5%

790 decrease for this experiment and an average decrease of 11% across all experiments at the highest

791 photochemical exposure. Increasing the equivalent OA mass concentration for the OFR walls to 100 and

792 1000 mg m^{-3} seemed to have no influence on model predictions. These findings imply that vapor wall

793 losses in the presence of sufficient seed aerosol might not be of concern for OFRs (Lambe et al., 2015).

794

795 ***Residence Time Distributions.*** Model simulations performed in this work assumed that the OFR operated

796 as a plug flow reactor with a constant residence time. Experimental studies by Lambe et al. (2011) and

797 fluid dynamics simulations by Ortega et al. (2016) have shown that OFRs, particularly like the one used

798 in this work, exhibit heterogeneity in residence times. We performed simulations to explore the sensitivity

799 of varying residence times on model predictions. These simulations were performed based on a

800 discretized version of the residence time distribution measured by Lambe et al. (2011) for SO$_2$ that

801 yielded an average residence time of 100 seconds (same as that used by Jathar et al. (2017a)). The

802 discretized version included six parcels with volume fractions of 0.23, 0.36, 0.24, 0.11, 0.05, and 0.01

803 with residence times of 45, 65, 100, 200, 300, and 500 seconds respectively. Each parcel experienced the

804 same OH concentration but the varying residence times resulted in different OH exposures for each

805 parcel. The parcels were combined after photochemical exposure without repartitioning the OA between

806 the six parcels. Similar to the findings of Peng et al. (2015) for calculating OH exposure, our results in

807 Figure 7(c) show that using a residence time distribution had very little influence on the OA mass

808 evolution compared to use of an effective average time. Compared to the base case, the residence time

809 distribution resulted in an average decrease of 3% and 5% in OA mass for the VBS and SOM models

810 respectively for all experiments at the highest photochemical exposure.

811

812 ***Spatial Heterogeneity in OH.*** In addition to the influence exerted by a distribution of residence times,

813 spatial heterogeneity in the gas-phase chemistry inside the OFR (e.g., from radial variation in light

814 intensity) could lead to spatial heterogeneity in OH concentrations and result in a distribution of OH

815 exposures for the sample being aged. We performed simulations to explore the sensitivity of a varying

816 OH exposure on model predictions. These simulations were performed where we split the sample coming

817   into the OFR into two parcels and treated the parcels to different OH exposures. Each experiment was

818   repeated for all combinations (six total) of three different parcel splits (¼-¾, ⅓-⅔, ½-½) and two different

819   OH exposure splits (⅓-X, ⅔-X); X was determined by conserving the total OH exposure reported by

820   Jathar et al. (2017a). For instance, the first simulation was performed by splitting the OFR air parcel into

821   ¼ and ¾ fractions by volume and exposing the ¼ volume to ⅓ the OH exposure. The parcels were

822   combined after photochemical exposure without repartitioning the OA between the two parcels. The

823   results in Figure 7(d) show that the simulated spatial heterogeneity always reduced the OA mass although

824   the maximum reduction (13% for the VBS and 14% for the SOM models) at the highest photochemical

825   exposure was within the measurement uncertainty at least for the SOM. Compared to the base case, the

826   spatial heterogeneity in OH resulted in a maximum decrease of 13% and 15% in OA mass for the VBS

827   and SOM models respectively for all experiments at the highest photochemical exposure.

828

829   **4. Summary and Discussion**

830   Recently, Jathar et al. (2017a) reported on experiments performed using the oxidation flow reactor (OFR)

831   to measure the photochemical production of secondary organic aerosol (SOA) from diesel exhaust under

832   varying engine loads, fuel types, and aftertreatment systems. These data present an opportunity to not only

833   test SOA models but also use these models to interpret OFR data and determine their relevance for the

834   real atmosphere. In this work, we applied two different SOA model frameworks (VBS and SOM) to

835   simulate the photochemical production of SOA in an OFR from diesel exhaust and evaluated those model

836   frameworks using the data from Jathar et al. (2017a). The volatility basis set (VBS) model is a

837   parameterized model that allows for a volatility-based representation of OA while the statistical oxidation

838   model (SOM) is a semi-explicit parameterized model that uses a carbon-oxygen grid to track OA. Both

839   simulated the coupled chemistry, thermodynamic properties, and gas/particle partitioning of OA and

840   accounted for: (i) semi-volatile and reactive emissions of primary organic aerosol (POA), (ii) SOA

841   production from IVOCs and VOCs, (iii) multi-generational aging, and (iv) kinetic gas/particle

842   partitioning.

843

844   Model predictions suggest that the instantaneous gas/particle partitioning assumption may over-predict

845   SOA formation in OFRs when the initial condensational sinks are low and the condensation of SOA is

846   likely kinetically limited. Hence, SOA formation in OFRs needs to be modeled/interpreted through an

847   explicit treatment of kinetic gas/particle partitioning. Differences in model predictions between

848   instantaneous and kinetic partitioning will depend on the rate at which condensable SOA mass is

849   produced in the OFR (depends on the initial precursor concentrations and photochemical exposure),

850   residence time in the OFR, properties of the condensing species (e.g., diffusion coefficient, molecular

851   weight), and parameters relevant for partitioning (e.g., accommodation coefficient, seed aerosol surface

852   area). To explore the relative importance of instantaneous and kinetically-limited partitioning in an OFR,

853   we used the SOM to simulate SOA formation from diluted diesel exhaust using instantaneous and kinetic

854   partitioning assumptions for varying amounts of SOA formed (1-10000 $\mu g\ m^{-3}$) and initial condensational

855   sinks (0.001-10 min^{-1}). These simulations were similar to the calculations performed by Palm et al. (2017)

856   where they calculated timescales and losses of condensable SOA vapors to the OFR walls and sampling

857   lines and reaction with OH. The calculations were performed for two different initial particle sizes (10

858   and 100 nm) since the condensation of SOA mass would grow the initial condensational sink for the two

859   particles at different rates, i.e. for the same starting initial condensational sink, smaller particles would

860   experience quicker growth in the condensational sink compared to larger particles for the same amount of

861   condensing mass. The calculations were also performed for two different residence times – 2 and 4

862   minutes – to span the residence time range used in typical applications of the OFR. We assumed an

863   accommodation coefficient of 0.1. The results plotted in Figure 8 show the ratio of SOA predicted

864   through kinetic partitioning to that predicted through instantaneous partitioning as a function of the initial

865   condensational sink and the SOA formed under an instantaneous partitioning assumption. Across the four

866   scenarios explored (two initial particle sizes and two residence times), the SOA formation predicted under

867   the kinetic partitioning assumption was an order of magnitude or more lower than that predicted under the

868   instantaneous partitioning assumption over a large portion of the input range explored, e.g., when the

869   initial condensational sink was smaller than ~0.1 min^{-1} and the maximum SOA formed was lower than

870   ~100 $\mu g\ m^{-3}$ for the 10 nm simulations and lower than ~1000 $\mu g\ m^{-3}$ for the 100 nm simulations. We also

871   found that the SOA formation in the OFR was kinetically-limited under typical ambient conditions. The

872   SOA formation predicted under the kinetic partitioning assumption approached the SOA formed under the

873   instantaneous partitioning assumption either when the initial condensational sink was very large (>5 min^{-}

874   ^{1}) or when a large amount of condensable SOA was produced in the OFR (>=1000 $\mu g\ m^{-3}$ for the 10 nm

875   particles and >>10000 $\mu g\ m^{-3}$ for the 100 nm particles). Our finding implies that ambient applications of

876   the OFR, where initial condensational sinks are typically smaller (~0.005-0.5 min^{-1}) and the maximum

877   SOA produced is typically less than 40 $\mu g\ m^{-3}$, will only produce a small fraction (0-30%) of the intended

878   SOA. Furthermore, our simulations suggested that a smaller initial particle size (i.e., 10 nm) for the same

879   initial condensational sink and a longer OFR residence time (i.e., 4 min) may not necessarily help produce

880   the intended SOA under ambient conditions. Although these simulation results need to be verified

881   experimentally, they do suggest that it might be challenging to operate the OFR in conditions where

882   instantaneous or atmospherically-relevant partitioning is applicable, further complicating the coupled

883   atmospheric simulation of chemistry and thermodynamics in OFRs.

884

885   Upon including IVOCs as SOA precursors, both the VBS and SOM models were able to reasonably

886   predict the OA mass evolution reported by Jathar et al. (2017a) across different engine loads, fuel types,

887   and aftertreatment systems. Model predictions suggest that 30% of the unburned hydrocarbon emissions

888   are likely IVOCs and that these IVOCs (regardless of the emissions profiles used to determine non-IVOC

889   emissions) account for most (average of 70%) of the SOA formed from diesel exhaust. These findings are

890   consistent with prior work from chamber experiments (Jathar et al., 2014b) and modeling studies (Zhao et

891   al., 2015). Simulations performed using single surrogates suggest that the complex mixture of IVOCs in

892   diesel exhaust could be well represented using a linear C_{13} or C_{15} alkane for the SOM but might need a

893   larger surrogate such as a C_{19} alkane for the VBS model. The need for a different surrogate species to

894   model IVOC SOA between the SOM and VBS models most likely arises from differences in the coupled

895   treatment of the oxidation chemistry and gas/particle partitioning in the OFR. The use of surrogates offers

896   a computationally-efficient strategy to model SOA formation from IVOCs in large-scale three-

897   dimensional models. The SOM tracks the carbon and oxygen numbers of the oxidation products and

898   hence model predictions were used to calculate atomic O:C ratios for OA, which were then compared to

899   measurements. While the inclusion of IVOCs allowed for good model-measurement comparisons on OA

900   mass, the SOM under-predicted the O:C ratio of OA on average by 28%, possibly highlighting the

901   limitations in modeling the IVOCs as alkanes and/or extrapolating chamber-based parameterizations to

902   OFR experiments. Model predictions of the gas-phase organic species compared favorably to those

903   measured using a chemical ionization mass spectrometer (CIMS), which qualitatively validates the

904   statistical evolution of organic compounds tracked through the generalized SOM mechanism.

905

906   As OFRs are increasingly used to study SOA formation and evolution in laboratory and field

907   environments, there is a need to develop models that can be used to interpret OFR data. This work

908   suggests that multi-generational aging (in case of the VBS model), residence time distributions, and

909   spatial heterogeneity in OH concentrations produced sensitivities that were well within the measurement

910   uncertainty and were not a concern for the model system studied. However, model predictions did appear

911   to be more sensitive to multi-generational aging (in case of the SOM) and influence of vapor wall losses,

912   highlighting that these processes be included in OFR models. While the conclusions from this work may

913   be relevant for other laboratory and ambient studies, their relative importance may vary. There are several

914   instances where the model development was insufficient and will likely be addressed in future work. For

915   example, the model could benefit from the use of a polydisperse size distribution to treat new particle

916 formation and growth and improve predictions of the evolution of the aerosol size distribution. Similarly,

917 the model needs to be rigorously tested against other laboratory (e.g., Lambe et al. (2012)) and ambient

918 (e.g., Palm et al. (2016)) OFR data.

919

5 Acknowledgements

921 We thank Dr. Zhe Peng and Dr. Jose Jimenez for running their oxidation flow reactor model (Peng and

922 Jimenez, 2017) to provide NO_X relevant inputs for our work. We thank the Dr. Jeffrey Pierce and Dr.

923 John Volckens for their feedback on the written manuscript. DKF acknowledges the Beckman Young

924 Investigator Award for funding.

925

6 References

927   Ahlberg, E., Falk, J., Eriksson, A., Holst, T., Brune, W. H., Kristensson, A., Roldin, P., and Svenningsson, B.:

928 Secondary organic aerosol from VOC mixtures in an oxidation flow reactor, Atmospheric environment, 161, 210-220, 2017.

929   Ahmadov, R., McKeen, S. A., Robinson, A. L., Bahreini, R., Middlebrook, A. M., de Gouw, J. A., Meagher, J., Hsie,

930 E. Y., Edgerton, E., Shaw, S., and Trainer, M.: A volatility basis set model for summertime secondary organic aerosols over

931 the eastern United States in 2006, Journal Of Geophysical Research-Atmospheres, 117, D06301, 2012.

932   Anderson, J. O., Thundiyil, J. G., and Stolbach, A.: Clearing the air: a review of the effects of particulate matter air

933 pollution on human health, Journal of Medical Toxicology, 8, 166-175, 2012.

934   Atkinson, R., and Arey, J.: Atmospheric degradation of volatile organic compounds, Chemical Reviews, 103, 4605-

935 4638, 2003.

936   Bond, T., Venkataraman, C., and Masera, O.: Global atmospheric impacts of residential fuels, Energy for Sustainable

937 Development, 8, 20-32, 2004.

938   Cappa, C., and Wilson, K.: Multi-generation gas-phase oxidation, equilibrium partitioning, and the formation and

939 evolution of secondary organic aerosol, Atmospheric Chemistry and Physics, 12, 9505-9528, 2012.

940   Cappa, C. D., Zhang, X., Loza, C. L., Craven, J. S., Yee, L. D., and Seinfeld, J. H.: Application of the Statistical

941 Oxidation Model (SOM) to Secondary Organic Aerosol formation from photooxidation of C 12 alkanes, Atmospheric

942 Chemistry and Physics, 13, 1591-1606, 2013.

943   Cappa, C. D., Jathar, S. H., Wexler, A. S., Seinfeld, J., and Kleeman, M. J.: Simulating secondary organic aerosol in a

944 regional air quality model using the statistical oxidation model – Part 2: Assessing the influence of vapor wall losses,

945 Atmospheric Chemistry & Physics, 16, 3041-3059, 2016.

946   Chacon-Madrid, H., and Donahue, N.: Fragmentation vs. functionalization: chemical aging and organic aerosol

947 formation, Atmos. Chem. Phys, 11, 10553-10563, doi:10.5194/acp-11-10553-2011 2011.

948   Chan, A. W. H., Kautzman, K. E., Chhabra, P. S., Surratt, J. D., Chan, M. N., Crounse, J. D., Kurten, A., Wennberg,

949 P. O., Flagan, R., and Seinfeld, J. H.: Secondary organic aerosol formation from photooxidation of naphthalene and

950 alkylnaphthalenes: implications for oxidation of intermediate volatility organic compounds (IVOCs), Atmospheric Chemistry

951 and Physics, 9, 3049-3060, 2009.

952   Chen, S., Brune, W., Lambe, A., Davidovits, P., and Onasch, T.: Modeling organic aerosol from the oxidation of

953   alpha-pinene in a Potential Aerosol Mass (PAM) chamber, Atmospheric Chemistry and Physics, 13, 5017-5031, 2013.

954   Chirico, R., DeCarlo, P., Heringa, M., Tritscher, T., Richter, R., Prevot, A., Dommen, J., Weingartner, E., and Wehrle,
955   G.: Impact of aftertreatment devices on primary emissions and secondary organic aerosol formation potential from in-use
956   diesel vehicles: results from smog chamber experiments, Atmospheric Chemistry and Physics, 10, 11545-11563, 2010.

957   Donahue, N., Robinson, A., Stanier, C., and Pandis, S.: Coupled partitioning, dilution, and chemical aging of
958   semivolatile organics, Environ. Sci. Technol, 40, 2635-2643, doi:10.1021/es052297c, 2006a.

959   Donahue, N., Epstein, S., Pandis, S., and Robinson, A.: A two-dimensional volatility basis set: 1. organic-aerosol
960   mixing thermodynamics, Atmospheric Chemistry and Physics, 11, 3303-3318, 2011.

961   Donahue, N. M., Robinson, A. L., Stanier, C. O., and Pandis, S. N.: Coupled partitioning, dilution, and chemical aging
962   of semivolatile organics., Environ. Sci. Technol., 40, 2635-2643, 2006b.

963   Dzepina, K., Volkamer, R., Madronich, S., Tulet, P., Ulbrich, I., Zhang, Q., Cappa, C., Ziemann, P., and Jimenez, J.:
964   Evaluation of recently-proposed secondary organic aerosol models for a case study in Mexico City, Atmospheric Chemistry
965   and Physics, 9, 5681-5709, doi:10.5194/acp-9-5681-2009, 2009.

966   Ensberg, J. J., Hayes, P. L., Jimenez, J. L., Gilman, J. B., Kuster, W. C., de Gouw, J. A., Holloway, J. S., Gordon, T.
967   D., Jathar, S., and Robinson, A. L.: Emission factor ratios, SOA mass yields, and the impact of vehicular emissions on SOA
968   formation, Atmospheric Chemistry and Physics, 14, 2383-2397, 2014.

969   EPA: SPECIATE Version 4.3, in, 2013.

970   EPA: Estimation Programs Interface Suite™. , in, United States Environmental Protection Agency, Washington, DC,
971   USA., 2017.

972   Friedman, B., Brophy, P., Brune, W. H., and Farmer, D. K.: Anthropogenic Sulfur Perturbations on Biogenic
973   Oxidation: SO2 Additions Impact Gas-Phase OH Oxidation Products of α- and β-Pinene, Environ. Sci. Technol., 50, 1269-
974   1279, 10.1021/acs.est.5b05010, 2016.

975   Friedman, B., Link, M. F., Fulgham, S. R., Brophy, P., Galang, A., Brune, W. H., Jathar, S. H., and Farmer, D. K.:
976   Primary and Secondary Sources of Gas-Phase Organic Acids from Diesel Exhaust, Environ. Sci. Technol., 51, 10872-10880,
977   10.1021/acs.est.7b01169, 2017.

978   Fuzzi, S., Baltensperger, U., Carslaw, K., Decesari, S., Denier van der Gon, H., Facchini, M. C., Fowler, D., Koren, I.,
979   Langford, B., Lohmann, U., Nemitz, E., Pandis, S., Riipinen, I., Rudich, Y., Schaap, M., Slowik, J. G., Spracklen, D. V.,
980   Vignati, E., Wild, M., Williams, M., and Gilardoni, S.: Particulate matter, air quality and climate: lessons learned and future
981   needs, Atmos. Chem. Phys., 15, 8217-8299, 10.5194/acp-15-8217-2015, 2015.

982   Gentner, D. R., Jathar, S. H., Gordon, T. D., Bahreini, R., Day, D. A., El Haddad, I., Hayes, P. L., Pieber, S. M., Platt,
983   S. M., and de Gouw, J. A.: A review of urban secondary organic aerosol formation from gasoline and diesel motor vehicle
984   emissions, Environ. Sci. Technol., 2016.

985   Gordon, T. D., Nguyen, N. T., Presto, A. A., Lipsky, E. M., Maldonado, S., Maricq, M., and Robinson, A. L.:
986   Secondary organic aerosol production from diesel vehicle exhaust: impact of aftertreatment, fuel chemistry and driving cycle,
987   Atmospheric Chemistry & Physics, 14, 4643-4659, doi:10.5194/acp-14-4643-2014, 2014.

988   Hayes, P., Carlton, A., Baker, K., Ahmadov, R., Washenfelder, R., Alvarez, S., Rappenglück, B., Gilman, J., Kuster,
989   W., and de Gouw, J.: Modeling the formation and aging of secondary organic aerosols in Los Angeles during CalNex 2010,
990   Atmospheric Chemistry and Physics, 15, 5773-5801, 2015.

991   Hildebrandt, L., Donahue, N., and Pandis, S.: High formation of secondary organic aerosol from the photo-oxidation

of toluene, Atmospheric Chemistry and Physics, 9, 2973-2986, doi:10.5194/acp-9-2973-2009, 2009.

Hodzic, A., Jimenez, J., Madronich, S., Canagaratna, M., DeCarlo, P., Kleinman, L., and Fast, J.: Modeling organic aerosols in a megacity: potential contribution of semi-volatile and intermediate volatility primary organic compounds to secondary organic aerosol formation, Atmospheric Chemistry and Physics, 10, 5491-5514, doi:10.5194/acp-10-5491-2010, 2010.

Huffman, J., Docherty, K., Mohr, C., Cubison, M., Ulbrich, I., Ziemann, P., Onasch, T., and Jimenez, J.: Chemically-resolved volatility measurements of organic aerosol from different sources, Environ. Sci. Technol., 43, 5351-5357, 2009.

Jathar, S., Farina, S., Robinson, A., and Adams, P.: The influence of semi-volatile and reactive primary emissions on the abundance and properties of global organic aerosol, Atmospheric Chemistry and Physics, 11, 7727-7746, doi:10.5194/acp-11-7727-2011 2011.

Jathar, S. H., Donahue, N. M., Adams, P. J., and Robinson, A. L.: Testing secondary organic aerosol models using smog chamber data for complex precursor mixtures: influence of precursor volatility and molecular structure, Atmospheric Chemistry and Physics, 14, 5771-5780, 2014a.

Jathar, S. H., Gordon, T. D., Hennigan, C. J., Pye, H. O. T., Pouliot, G. A., Adams, P. J., Donahue, N. M., and Robinson, A. L.: Unspeciated organic emissions from combustion sources and their influence on the secondary organic aerosol budget in the United States, Proceedings of the National Academy of Sciences, 111, 10473-10478, 2014b.

Jathar, S. H., Cappa, C. D., Wexler, A. S., Seinfeld, J. H., and Kleeman, M. J.: Multi-generational oxidation model to simulate secondary organic aerosol in a 3-D air quality model, Geosci. Model Dev., 8, 2553-2567, 10.5194/gmd-8-2553-2015, 2015.

Jathar, S. H., Cappa, C. D., Wexler, A. S., Seinfeld, J. H., and Kleeman, M. J.: Simulating secondary organic aerosol in a regional air quality model using the statistical oxidation model – Part 1: Assessing the influence of constrained multi-generational ageing, Atmospheric Chemistry & Physics, 16, 2309-2322, 2016.

Jathar, S. H., Friedman, B., Galang, A. A., Link, M. F., Brophy, P., Volckens, J., Eluri, S., and Farmer, D. K.: Linking Load, Fuel and Emission Controls to Photochemical Production of Secondary Organic Aerosol from a Diesel Engine, Environ. Sci. Technol., 2017a.

Jathar, S. H., Woody, M., Pye, H. O., Baker, K. R., and Robinson, A. L.: Chemical transport model simulations of organic aerosol in southern California: model evaluation and gasoline and diesel source contributions, Atmospheric Chemistry and Physics, 17, 4305-4318, 2017b.

Karnezi, E., Riipinen, I., and Pandis, S.: Measuring the atmospheric organic aerosol volatility distribution: a theoretical analysis, Atmospheric Measurement Techniques, 7, 2953-2965, 2014.

Konovalov, I. B., Beekmann, M., Berezin, E. V., Petetin, H., Mielonen, T., Kuznetsova, I. N., and Andreae, M. O.: The role of semi-volatile organic compounds in the mesoscale evolution of biomass burning aerosol: a modelling case study of the 2010 mega-fire event in Russia, Atmospheric Chemistry and Physics Discussions, 15, 9107-9172, 2015.

Krechmer, J. E., Pagonis, D., Ziemann, P. J., and Jimenez, J. L. L.: Quantification of gas-wall partitioning in Teflon environmental chambers using rapid bursts of low-volatility oxidized species generated in-situ, Environ. Sci. Technol., 2016.

Krechmer, J. E., Day, D. A., Ziemann, P. J., and Jimenez, J. L.: Direct measurements of gas/particle partitioning and mass accommodation coefficients in environmental chambers, Environ. Sci. Technol., 51, 11867-11875, 2017.

Kroll, J. H., Smith, J. D., Che, D. L., Kessler, S. H., Worsnop, D. R., and Wilson, K. R.: Measurement of fragmentation and functionalization pathways in the heterogeneous oxidation of oxidized organic aerosol, Physical Chemistry

031 Chemical Physics, 11, 8005-8014, 2009.

032   Lambe, A., Chhabra, P., Onasch, T., Brune, W., Hunter, J., Kroll, J., Cummings, M., Brogan, J., Parmar, Y., and
033 Worsnop, D.: Effect of oxidant concentration, exposure time, and seed particles on secondary organic aerosol chemical
034 composition and yield, Atmospheric Chemistry and Physics, 15, 3063-3075, 2015.

035   Lambe, A. T., Ahern, A. T., Williams, L. R., Slowik, J. G., Wong, J. P. S., Abbatt, J. P. D., Brune, W. H., Ng, N. L.,
036 Wright, J. P., and Croasdale, D. R.: Characterization of aerosol photooxidation flow reactors: heterogeneous oxidation,
037 secondary organic aerosol formation and cloud condensation nuclei activity measurements, Atmospheric Measurement
038 Techniques, 4, 445-461, 2011.

039   Lambe, A. T., Onasch, T. B., Croasdale, D. R., Wright, J. P., Martin, A. T., Franklin, J. P., Massoli, P., Kroll, J. H.,
040 Canagaratna, M. R., and Brune, W. H.: Transitions from functionalization to fragmentation reactions of laboratory secondary
041 organic aerosol (SOA) generated from the OH oxidation of alkane precursors, Environ. Sci. Technol., 46, 5430-5437, 2012.

042   Lee, B.-H., Pierce, J. R., Engelhart, G. J., and Pandis, S. N.: Volatility of secondary organic aerosol from the
043 ozonolysis of monoterpenes, Atmospheric environment, 45, 2443-2452, 2011.

044   Lim, Y. B., and Ziemann, P. J.: Effects of molecular structure on aerosol yields from OH radical-initiated reactions of
045 linear, branched, and cyclic alkanes in the presence of NO x, Environ. Sci. Technol., 43, 2328-2334, 2009.

046   Link, M., Friedman, B., Fulgham, R., Brophy, P., Galang, A., Jathar, S., Veres, P., Roberts, J., and Farmer, D.:
047 Photochemical processing of diesel fuel emissions as a large secondary source of isocyanic acid (HNCO), Geophysical
048 Research Letters, 43, 4033-4041, 2016.

049   May, A. A., Levin, E. J. T., Hennigan, C. J., Riipinen, I., Lee, T., Collett, J. L., Jimenez, J. L., Kreidenweis, S. M., and
050 Robinson, A. L.: Gas-particle partitioning of primary organic aerosol emissions: 3. Biomass burning, Journal of Geophysical
051 Research: Atmospheres, 118, 2013JD020286, 10.1002/jgrd.50828, 2013a.

052   May, A. A., Presto, A. A., Hennigan, C. J., Nguyen, N. T., Gordon, T. D., and Robinson, A. L.: Gas-particle
053 partitioning of primary organic aerosol emissions: (2) Diesel vehicles, Environ. Sci. Technol., 47, 8288-8296, 2013b.

054   May, A. A., Presto, A. A., Hennigan, C. J., Nguyen, N. T., Gordon, T. D., and Robinson, A. L.: Gas-particle
055 partitioning of primary organic aerosol emissions: (1) gasoline vehicle exhaust, Atmospheric Environment, 77, 128-139,
056 2013c.

057   Murphy, B., and Pandis, S.: Simulating the formation of semivolatile primary and secondary organic aerosol in a
058 regional chemical transport model., Environ. Sci. Technol., 43, 4722-4728, doi:10.1021/es803168a, 2009.

059   Ng, N., Kroll, J., Chan, A., Chhabra, P., Flagan, R., and Seinfeld, J.: Secondary organic aerosol formation from m-
060 xylene, toluene, and benzene, Atmos. Chem. Phys, 7, 3909-3922, doi:10.5194/acp-7-3909-2007, 2007.

061   Odum, J. R., Hoffmann, T., Bowman, F., Collins, D., Flagan, R. C., and Seinfeld, J. H.: Gas/particle partitioning and
062 secondary organic aerosol yields, Environ. Sci. Technol., 30, 2580-2585, 1996.

063   Ortega, A. M., Hayes, P. L., Peng, Z., Palm, B. B., Hu, W., Day, D. A., Li, R., Cubison, M. J., Brune, W. H., and
064 Graus, M.: Real-time measurements of secondary organic aerosol formation and aging from ambient air in an oxidation flow
065 reactor in the Los Angeles area, Atmospheric Chemistry and Physics, 16, 7411-7433, 2016.

066   Pachauri, R. K., Allen, M. R., Barros, V. R., Broome, J., Cramer, W., Christ, R., Church, J. A., Clarke, L., Dahe, Q.,
067 Dasgupta, P., Dubash, N. K., Edenhofer, O., Elgizouli, I., Field, C. B., Forster, P., Friedlingstein, P., Fuglestvedt, J., Gomez-
068 Echeverri, L., Hallegatte, S., Hegerl, G., Howden, M., Jiang, K., Jimenez Cisneroz, B., Kattsov, V., Lee, H., Mach, K. J.,
069 Marotzke, J., Mastrandrea, M. D., Meyer, L., Minx, J., Mulugetta, Y., O'Brien, K., Oppenheimer, M., Pereira, J. J., Pichs-

070   Madruga, R., Plattner, G. K., Pörtner, H.-O., Power, S. B., Preston, B., Ravindranath, N. H., Reisinger, A., Riahi, K.,

071   Rusticucci, M., Scholes, R., Seyboth, K., Sokona, Y., Stavins, R., Stocker, T. F., Tschakert, P., van Vuuren, D., and van

072   Ypserle, J. P.: Climate Change 2014: Synthesis Report. Contribution of Working Groups I, II and III to the Fifth Assessment

073   Report of the Intergovernmental Panel on Climate Change, edited by: Pachauri, R. K., and Meyer, L., IPCC, Geneva,

074   Switzerland, 151 pp., 2014.

075   Palm, B. B., Campuzano-Jost, P., Ortega, A. M., Day, D. A., Kaser, L., Jud, W., Karl, T., Hansel, A., Hunter, J. F.,

076   and Cross, E. S.: In situ secondary organic aerosol formation from ambient pine forest air using an oxidation flow reactor,

077   Atmospheric Chemistry and Physics, 16, 2943-2970, 2016.

078   Pankow, J. F.: An absorption model of gas/particle partitioning of organic compounds in the atmosphere, Atmospheric

079   Environment, 28, 185-188, 1994.

080   Pankow, J. F., and Barsanti, K. C.: The carbon number-polarity grid: A means to manage the complexity of the mix of

081   organic compounds when modeling atmospheric organic particulate matter, Atmospheric Environment, 43, 2829-2835, 2009.

082   Peng, Z., Day, D., Stark, H., Li, R., Lee-Taylor, J., Palm, B., Brune, W., and Jimenez, J.: HOx radical chemistry in

083   oxidation flow reactors with low-pressure mercury lamps systematically examined by modeling, Atmospheric Measurement

084   Techniques, 8, 4863-4890, 2015.

085   Presto, A. A., Miracolo, M. A., Donahue, N. M., and Robinson, A. L.: Secondary organic aerosol formation from

086   high-NO x photo-oxidation of low volatility precursors: n-alkanes, Environ. Sci. Technol., 44, 2029-2034, 2010.

087   Presto, A. A., Nguyen, N. T., Ranjan, M., Reeder, A. J., Lipsky, E. M., Hennigan, C. J., Miracolo, M. A., Riemer, D.

088   D., and Robinson, A. L.: Fine particle and organic vapor emissions from staged tests of an in-use aircraft engine, Atmospheric

089   Environment, 45, 3603-3612, 2011.

090   Pye, H., and Seinfeld, J.: A global perspective on aerosol from low-volatility organic compounds, Atmos. Chem.

091   Phys, 10, 4377-4401, doi:10.5194/acp-10-4377-2010, 2010.

092   Robinson, A. L., Donahue, N. M., Shrivastava, M. K., Weitkamp, E. A., Sage, A. M., Grieshop, A. P., Lane, T. E.,

093   Pierce, J. R., and Pandis, S. N.: Rethinking organic aerosols: Semivolatile emissions and photochemical aging, Science, 315,

094   1259-1262, 2007.

095   Saleh, R., Donahue, N. M., and Robinson, A. L.: Time scales for gas-particle partitioning equilibration of secondary

096   organic aerosol formed from alpha-pinene ozonolysis, Environ. Sci. Technol., 47, 5588-5594, 2013.

097   Seinfeld, J. H., and Pandis, S. N.: Atmospheric Chemistry and Physics, John Wiley and Sons., New York, 2006.

098   Simonen, P., Saukko, E., Karjalainen, P., Timonen, H., Bloss, M., Aakko-Saksa, P., Rönkkö, T., Keskinen, J., and Dal

099   Maso, M.: A new oxidation flow reactor for measuring secondary aerosol formation of rapidly changing emission sources,

100   Atmospheric Measurement Techniques, 10, 1519, 2017.

101   Song, C., Na, K., Warren, B., Malloy, Q., and Cocker III, D. R.: Secondary organic aerosol formation from the

102   photooxidation of p-and o-xylene, Environ. Sci. Technol., 41, 7403-7408, 2007.

103   Tkacik, D. S., Presto, A. A., Donahue, N. M., and Robinson, A. L.: Secondary organic aerosol formation from

104   intermediate-volatility organic compounds: cyclic, linear, and branched alkanes, Environ. Sci. Technol., 46, 8773-8781, doi:

105   10.1021/es301112c, 2012.

106   Tkacik, D. S., Lambe, A. T., Jathar, S., Li, X., Presto, A. A., Zhao, Y., Blake, D., Meinardi, S., Jayne, J. T., Croteau,

107   P. L., and Robinson, A. L.: Secondary Organic Aerosol Formation from in-Use Motor Vehicle Emissions Using a Potential

108   Aerosol Mass Reactor, Environ. Sci. Technol., 48, 11235-11242, 10.1021/es502239v, 2014.

109   Tsimpidi, A., Karydis, V., Zavala, M., Lei, W., Molina, L., Ulbrich, I., Jimenez, J., and Pandis, S.: Evaluation of the

110   volatility basis-set approach for the simulation of organic aerosol formation in the Mexico City metropolitan area, Atmos.

111   Chem. Phys, 10, 525-546, doi:10.5194/acp-10-525-2010, 2009.

112   Zhang, X., Cappa, C. D., Jathar, S. H., McVay, R. C., Ensberg, J. J., Kleeman, M. J., and Seinfeld, J. H.: Influence of

113   vapor wall loss in laboratory chambers on yields of secondary organic aerosol, Proceedings of the National Academy of

114   Sciences, 111, 5802-5807, 2014.

115   Zhao, Y., Nguyen, N. T., Presto, A. A., Hennigan, C. J., May, A. A., and Robinson, A. L.: Intermediate volatility

116   organic compound emissions from on-road diesel vehicles: chemical composition, emission factors, and estimated secondary

117   organic aerosol production, Environ. Sci. Technol., 49, 11516-11526, 2015.

118

119 7 Tables

120

121 *Table 1: Primary emissions of THC and POA, maximum photochemical production of SOA, maximum O:C of the OA, maximum OH exposure,*
122 *and size distribution data from Jathar et al. (2017a).*

Load-Fuel-Aftertreatment Experiment	Date	THC ($\mu g\ m^{-3}$)	CO (ppbv)	NO (ppbv)	NO_2 (ppbv)	POA ($\mu g\ m^{-3}$)	SOA[%] ($\mu g\ m^{-3}$)	O: C[%]	OH Exposure[%] (molec.-hr cm^{-3})	Number Mean Dia.[*] (nm)	Number Conc.[*] ($\#\ cm^{-3}$)
Idle-Diesel-None	June 3	1519	2746	960	318	38±15	209±66	0.23±0.01	2.1×10^7		8.0×10^5
	June 5	1810	5809	878	502	35±11	875±288	0.46±0.07	6.67×10^7	46	6.5×10^5
	June 12	2554	9664	1870	1103	85±17	877±277	0.57±0.09	3.61×10^7		3.4×10^5
Idle-Biodiesel-None	June 4	1118	4270	867	344	22±12	999±316	0.52±0.07	9.17×10^7	$46^@$	$7.3\times10^{5@}$
	June 8	2160	8169	1578	811	69±20	1415±468	0.36±0.03	4.72×10^7		$4.1\times10^{5@}$
Load-Diesel-None	June 3	959	1558	4999	379	19±11	181±58	0.37±0.01	3.6×10^7	190	5.3×10^5
	June 5	711	1400	6690	34	37±13	253±100	0.32±0.04	2.61×10^7		4.4×10^5
Load- Biodiesel-None	June 4	1634	1410	6364	30	29±18	645±204	0.38±0.05	2.78×10^7	$190^@$	$5.0\times10^{5@}$
	June 8	518	2051	10813	496	46±22	284±106	0.30±0.04	1.42×10^7		$3.3\times10^{5@}$
Idle-Diesel-DPF+DOC	June 9	2135	7473	2383	23	1.5±0.6	1040±335	0.37±0.02	5×10^7	52	910
Load-Diesel-DPF+DOC	June 9	303	85	6157	4483	1.6±3.6	146±48	0.29±0.01	1.31×10^7	57	968
Idle-Biodiesel-DPF+DOC	June 10	1773	7452	2213	182	2.6±1	787±250	0.44±0.04	5.28×10^7	$52^@$	$910^@$
Load-Biodiesel-DPF+DOC	June 10	261	58	5475	4525	2±0.14	107±9	0.29±0.01	1.39×10^7	$57^@$	$968^@$

123 DPF=diesel particulate filter, DOC=diesel oxidation catalyst
124 [%]maximum values measured in each experiment
125 [*]values measured at no OH exposure
126 [@]No data, assumed to be similar to the equivalent diesel experiment for the model

127   *Table 2: SOA precursors and mass yields used in the VBS model for high NO_X conditions.*

Species	$log_{10}C^*$					Reference
	0.1	*1*	*10*	*100*	*1000*	
toluene	0.0000	0.0100	0.2400	0.4500	0.7000	Hildebrandt et al. (2009)
benzene	0.0392	0.0315	0.0000	0.8230	0.0957	Ng et al. (2007)[#]
m-xylene	0.0032	0.0106	0.0633	0.0465	0.0000	Ng et al. (2007)[#]
p-xylene	0.0000	0.0022	0.0764	0.0000	0.0000	Song et al. (2007)[#]
o-xylene	0.0000	0.0132	0.1140	0.0000	0.0000	Song et al. (2007)[#]
naphthalene	0.0000	0.1660	0.0000	0.5400	0.8130	Chan et al. (2009)[#]
1-methylnaphthalene	0.0000	0.0170	0.4860	0.0000	0.0000	Chan et al. (2009)[#]
2-methylnaphthalene	0.0000	0.0531	0.5040	0.0000	0.0000	Chan et al. (2009)[#]
1,2-dimethylnaphthalene	0.0000	0.3100	0.0000	0.0000	0.0000	Chan et al. (2009)[#]
1-methyl-3-n-propylbenzene	0.0000	0.0000	0.0405	0.0694	0.1140	Odum et al. (1996)[#]
n-decane	0.0000	0.0000	0.0110	0.1280	0.2420	Presto et al. (2010)[&]
n-undecane	0.0000	0.0040	0.0720	0.1760	0.1450	Presto et al. (2010)[&]
n-dodecane	0.0000	0.0140	0.1100	0.1600	0.0000	Presto et al. (2010)[&]
n-tridecane	0.0140	0.0590	0.0940	0.0710	0.0000	Presto et al. (2010)[&]
n-tetradecane	0.0940	0.3000	0.3500	0.0000	0.0000	Presto et al. (2010)[&]
n-pentadecane	0.0440	0.0710	0.4100	0.3000	0.0000	Presto et al. (2010)[&]
n-hexadecane	0.0530	0.0830	0.4600	0.2500	0.0000	Presto et al. (2010)[&]
n-heptadecane	0.0630	0.0890	0.5500	0.2000	0.0000	Presto et al. (2010)[&]
n-octadecane	0.0760	0.3195	0.3750	0.1000	0.0000	Presto et al. (2010)[&]
n-nonadecane	0.0890	0.5500	0.2000	0.0000	0.0000	Presto et al. (2010)[&]
n-eicosane	0.3195	0.3750	0.1000	0.0000	0.0000	Presto et al. (2010)[&]
n-heneicosane	0.5500	0.2000	0.0000	0.0000	0.0000	Presto et al. (2010)[&]
n-docosane	0.3750	0.1000	0.0000	0.0000	0.0000	Presto et al. (2010)[&]

128   [&]extrapolated from the Presto et al. (2010) data
129   [#]do not account for vapor wall losses
130
131   *Table 3: SOA precursors and mass yields used in the VBS model for low NO_X conditions.*

Species	C^*					Reference
	0.1	*1*	*10*	*100*	*1000*	
toluene	0.0000	0.0100	0.2400	0.7000	0.7000	Hildebrandt et al. (2009)
benzene	0.0000	0.0000	0.0000	0.3700	0.0000	Ng et al. (2007)[#]
m-xylene	0.0000	0.0000	0.0000	0.0310	0.0000	Ng et al. (2007)[#]
p-xylene	0.0000	0.0000	0.0000	0.0310	0.0000	Ng et al. (2007)[#]
o-xylene	0.0000	0.0000	0.0000	0.0310	0.0000	Ng et al. (2007)[#]
naphthalene	0.0000	0.1565	0.0000	0.1199	0.2708	Chan et al. (2009)[#]
1-methylnaphthalene	0.0000	0.1565	0.0000	0.1199	0.2708	Chan et al. (2009)[#]
2-methylnaphthalene	0.0000	0.1565	0.0000	0.1199	0.2708	Chan et al. (2009)[#]
n-decane	0.0002	0.0050	0.0013	0.3938	0.0278	Loza et al. (2014)[&]
n-undecane	0.0001	0.0070	0.0216	0.3321	0.0000	Loza et al. (2014)[&]
n-dodecane	0.0011	0.0080	0.0279	0.3902	0.0003	Loza et al. (2014)[&]
n-tridecane	0.0029	0.0064	0.0551	0.3231	0.7090	Loza et al. (2014)[&]
n-tetradecane	0.0004	1.2000	0.1777	0.0194	0.0014	Loza et al. (2014)[&]
n-pentadecane	0.0032	0.0124	0.0686	0.5050	0.0025	Loza et al. (2014)[&]

n-hexadecane	0.0000	0.0572	0.2754	0.4346	0.1710	Loza et al. (2014)[&]
n-heptadecane	0.0399	0.0757	0.4409	0.3691	0.0000	Loza et al. (2014)[&]
n-octadecane	0.1958	0.0203	0.7077	0.0777	0.0000	Loza et al. (2014)[&]
n-nonadecane	1.0281	0.0000	0.0000	0.0000	0.0000	Loza et al. (2014)[&]
n-eicosane	0.0024	0.8470	0.2160	0.0000	0.0000	Loza et al. (2014)[&]
n-heneicosane	0.3629	0.6766	0.0250	0.0000	0.0000	Loza et al. (2014)[&]
n-docosane	0.7991	0.2633	0.0000	0.0000	0.0000	Loza et al. (2014)[&]
C_{12} branched alkane	0.0077	0.0015	0.0416	0.2486	0.9179	Loza et al. (2014)[&]
C_{13} branched alkane	0.0105	0.0007	0.0610	0.2376	1.2045	Loza et al. (2014)[&]
C_{14} branched alkane	0.0135	0.0007	0.0819	0.4173	0.4879	Loza et al. (2014)[&]
C_{15} branched alkane	0.0156	0.0034	0.1677	0.3553	0.7973	Loza et al. (2014)[&]
C_{16} branched alkane	0.0075	0.0704	0.1689	0.5741	0.0000	Loza et al. (2014)[&]
C_{17} branched alkane	0.0510	0.0000	0.4527	0.4605	0.0000	Loza et al. (2014)[&]
C_{18} branched alkane	0.0836	0.0001	0.7962	0.1484	0.0000	Loza et al. (2014)[&]
C_{19} branched alkane	0.3151	0.0001	0.7470	0.0000	0.0000	Loza et al. (2014)[&]
C_{20} branched alkane	0.0198	0.8698	0.1725	0.0000	0.0000	Loza et al. (2014)[&]
C_{21} branched alkane	0.3753	0.6837	0.0000	0.0000	0.0000	Loza et al. (2014)[&]
C_{22} branched alkane	0.8517	0.2056	0.0000	0.0000	0.0000	Loza et al. (2014)[&]
C_{12} cyclic alkane	0.0128	0.0302	0.0124	0.6156	0.0043	Loza et al. (2014)[&]
C_{13} cyclic alkane	0.0297	0.0000	0.0939	0.4062	1.0776	Loza et al. (2014)[&]
C_{14} cyclic alkane	0.0322	0.0000	0.1521	0.5341	0.5717	Loza et al. (2014)[&]
C_{15} cyclic alkane	0.0345	0.0000	0.3430	0.3231	0.8672	Loza et al. (2014)[&]
C_{16} cyclic alkane	0.0147	0.1426	0.3616	0.2839	0.6597	Loza et al. (2014)[&]
C_{17} cyclic alkane	0.0574	0.2408	0.3453	0.4060	0.0000	Loza et al. (2014)[&]
C_{18} cyclic alkane	0.2546	0.0643	0.6091	0.1431	0.0000	Loza et al. (2014)[&]
C_{19} cyclic alkane	0.2940	0.2790	0.5010	0.0000	0.0000	Loza et al. (2014)[&]
C_{20} cyclic alkane	0.3423	0.5700	0.1653	0.0000	0.0000	Loza et al. (2014)[&]
C_{21} cyclic alkane	0.6100	0.4478	0.0155	0.0000	0.0000	Loza et al. (2014)[&]
C_{22} cyclic alkane	0.9573	0.1110	0.0013	0.0000	0.0000	Loza et al. (2014)[&]

[&]produced from pseudo chamber data generated using the SOM
[#]do not account for vapor wall losses

Table 4: SOA precursors and parameters used in the SOM (Cappa et al., 2016) for high NO_X conditions.

Species	m_{frag}	ΔLVP	$p_{O,1}$	$p_{O,2}$	$p_{O,3}$	$p_{O,4}$	Reference
n-dodecane	0.0980	1.3900	0.9270	0.0101	0.0180	0.0445	Loza et al. (2014)
methylundecane	0.0100	1.2100	0.7419	0.0011	0.1820	0.0750	Loza et al. (2014)
hexylcyclohexane	0.0477	1.5700	0.7313	0.0381	0.2101	0.0205	Loza et al. (2014)
toluene	0.2220	1.2400	0.0029	0.0010	0.0010	1.0100	Zhang et al. (2014)
benzene	0.5350	1.7000	0.0792	0.0010	0.9190	0.0010	Ng et al. (2007)
m-xylene	0.0100	1.6800	0.9360	0.0010	0.0021	0.0609	Ng et al. (2007)
naphthalene	0.1210	1.3100	0.6440	0.0010	0.0460	0.3080	Chan et al. (2009)

Table 5: SOA precursors and parameters used in the SOM (Cappa et al., 2016) for low NO_X conditions.

Species	m_{frag}	ΔLVP	$p_{O,1}$	$p_{O,2}$	$p_{O,3}$	$p_{O,4}$	Reference
n-dodecane	2.0000	1.8300	0.9990	0.0010	0.0010	0.0010	Loza et al. (2014)

methylundecane	2.8200	1.9100	0.9980	0.0010	0.0010	0.0010	Loza et al. (2014)
hexylcyclohexane	5.0000	2.0500	0.8160	0.1810	0.0019	0.0010	Loza et al. (2014)
toluene	1.3100	1.7700	0.1850	0.0010	0.0019	0.8120	Zhang et al. (2014)
benzene	0.0807	1.9700	0.6370	0.0010	0.0021	0.3600	Ng et al. (2007)
m-xylene	1.0800	2.0500	0.1020	0.0010	0.8780	0.0190	Ng et al. (2007)
naphthalene	0.1890	1.8700	0.3520	0.0543	0.5330	0.0609	Chan et al. (2009)

138

139

140 *Table 6: (a) Volatility- and (b) carbon-number resolved distributions used to determine mass*
141 *concentrations of POC in the VBS and SOM models respectively. The volatility distributions are from*
142 *(May et al., 2013b)..*

C^* ($\mu g\ m^{-3}$)	10^{-2}	10^{-1}	10^{1}	10^{2}	10^{3}	10^{4}	10^{5}	10^{6}
f_i	0.03	0.25	0.37	0.23	0.06	0.03	0.01	0.01

143

Carbon No.	<16	16	17	18	19	20	21	22	23	24	25	26	>26
f_i	0.003	0.000	0.058	0.043	0.055	0.094	0.146	0.181	0.178	0.137	0.078	0.026	0.001

144

145 *Table 7: Reaction rate constants (k_{OH}), mass fractions, and VBS and SOM surrogates for SOA precursors*
146 *in diesel and biodiesel emissions. k_{OH} values are from Atkinson and Arey (2003) when available or the*
147 *EPI Suite version 4.11 (EPA, 2017).*

Species	Carbon Number	k_{OH} (cm^3 molecules^{-1} s^{-1})	Mass Percentage of THC		VBS Surrogate	SOM Surrogate
			Diesel	Biodiesel		
ethylbenzene	8	7.0×10^{-12}	0.2516	0.0826	toluene	toluene
indan	9	1.9×10^{-11}	0.1542	NA	naphthalene	naphthalene
butylbenzene	10	4.5×10^{-12}	0.0081	0.4720	*m*-xylene	*m*-xylene
diethylbenzene	10	8.11×10^{-12}	0.0731	NA	*m*-xylene	*m*-xylene
isopropyltoluene	10	8.54×10^{-12}	NA	0.3599	toluene	toluene
m-xylene	8	2.31×10^{-11}	0.4951	0.3717	*m*-xylene	*m*-xylene
o-xylene	8	1.36×10^{-11}	0.2760	0.3953	*o*-xylene	*m*-xylene
p-xylene	8	1.43×10^{-11}	0.0812	NA	*p*-xylene	*m*-xylene
n-decane	10	1.1×10^{-11}	0.4302	1.7050	*n*-decane	*n*-decane
n-undecane	11	1.23×10^{-11}	0.2110	1.9410	*n*-undecane	*n*-dodecane
toluene	7	5.63×10^{-12}	1.1932	1.6401	toluene	toluene
n-tridecane	13	1.68×10^{-11}	NA	0.6136	*n*-tridecane	*n*-dodecane
benzaldehyde	7	1.2×10^{-11}	0.5682	NA	benzene	benzene
benzene	6	1.22×10^{-12}	1.6234	1.5988	benzene	benzene
C_{10} aromatics	10	2.3×10^{-11}	0.0649	NA	*m*-xylene	*m*-xylene
C_9 aromatics	9	2.31×10^{-11}	0.4058	NA	*m*-xylene	*m*-xylene
1,2,3-trimethylbenzene	9	3.27×10^{-11}	0.0974	NA	*m*-xylene	*m*-xylene
1,2,4-trimethylbenzene	9	3.25×10^{-11}	0.4302	0.4720	*m*-xylene	*m*-xylene

1,2-diethylbenzene	10	8.11×10^{-12}	0.0731	NA	toluene	toluene
1,3,5-trimethylbenzene	9	5.67×10^{-11}	NA	0.1888	*m*-xylene	*m*-xylene
1,2-dimethyl-4-ethylbenzene	10	1.69×10^{-11}	NA	0.176	*m*-xylene	*m*-xylene
1,3-dimethyl-2-ethylbenzene	10	1.76×10^{-11}	NA	0.3304	*m*-xylene	*m*-xylene
1,4-dimethyl-2-ethylbenzene	10	1.69×10^{-11}	NA	0.4366	*m*-xylene	*m*-xylene
1-(1,1-dimethylethyl)-3,5-dimethylbenzene	12	3.01×10^{-11}	NA	0.3717	*m*-xylene	*m*-xylene
1-methyl-2-ethylbenzene	9	7.44×10^{-12}	0.1136	0.3835	toluene	toluene
1-methyl-3-ethylbenzene	9	1.39×10^{-11}	0.2029	0.7198	toluene	toluene
1-methyl-2-tert-butylbenzene	11	6.74×10^{-12}	NA	0.4307	toluene	toluene
1-tert-butyl-4-ethylbenzene	12	7.42×10^{-12}	NA	0.1947	*m*-xylene	*m*-xylene
2-methyl-butyl-benzene	11	1.02×10^{-11}	NA	1.1032	*m*-xylene	*m*-xylene
3,3-dimethyloctane	10	7.21×10^{-12}	NA	0.3068	*n*-decane	methylundecane
3-ethyloctane	10	1.18×10^{-11}	NA	0.1888	*n*-decane	methylundecane
3-methylnonane	10	1.14×10^{-11}	NA	0.2655	*n*-decane	methylundecane
C_{12} branched alkane	12	1.82×10^{-11}	1.1335	1.1335	*n*-decane	methylundecane
C_{13} branched alkane	13	1.68×10^{-11}	0.8111	0.8111	*n*-undecane	methylundecane
C_{14} branched alkane	14	1.39×10^{-11}	0.5257	0.5257	*n*-dodecane	methylundecane
C_{15} branched alkane	15	1.82×10^{-11}	0.4692	0.4692	*n*-tridecane	methylundecane
C_{16} branched alkane	16	1.96×10^{-11}	0.4935	0.4935	*n*-tetradecane	methylundecane
C_{17} branched alkane	17	2.1×10^{-11}	0.2198	0.2198	*n*-pentadecane	methylundecane
C_{18} branched alkane	18	2.24×10^{-11}	0.2863	0.2863	*n*-hexadecane	methylundecane
C_{19} branched alkane	19	2.38×10^{-11}	0.1716	0.1716	*n*-heptadecane	methylundecane
C_{20} branched alkane	20	2.52×10^{-11}	0.0969	0.0969	*n*-octadecane	methylundecane
C_{21} branched alkane	21	2.67×10^{-11}	0.0639	0.0639	*n*-nonadecane	methylundecane
C_{22} branched alkane	22	2.81×10^{-11}	0.0604	0.0604	*n*-eicosane	methylundecane
C_{12} cyclic alkane	12	1.82×10^{-11}	4.3427	4.3427	*n*-tetradecane	hexylcyclohexane
C_{13} cyclic alkane	13	1.68×10^{-11}	4.4265	4.4265	*n*-pentadecane	hexylcyclohexane
C_{14} cyclic alkane	14	1.39×10^{-11}	3.1480	3.1480	*n*-	hexylcyclohexane

					hexadecane	
C$_{15}$ cyclic alkane	15	1.82×10^{-11}	2.8599	2.8599	*n*-heptadecane	hexylcyclohexane
C$_{16}$ cyclic alkane	16	1.96×10^{-11}	2.1848	2.1848	*n*-octatadecane	hexylcyclohexane
C$_{17}$ cyclic alkane	17	2.1×10^{-11}	1.8546	1.8546	*n*-nonadecane	hexylcyclohexane
C$_{18}$ cyclic alkane	18	2.24×10^{-11}	1.6900	1.6900	*n*-eicosane	hexylcyclohexane
C$_{19}$ cyclic alkane	19	2.38×10^{-11}	1.0570	1.0570	*n*-heneicosane	hexylcyclohexane
C$_{20}$ cyclic alkane	20	2.52×10^{-11}	0.5900	0.5900	*n*-docosane	hexylcyclohexane
C$_{21}$ cyclic alkane	21	2.67×10^{-11}	0.3736	0.3736	*n*-tricosane	hexylcyclohexane
C$_{22}$ cyclic alkane	22	2.81×10^{-11}	0.3141	0.3141	*n*-tricosane	hexylcyclohexane
dodecane	12	1.82×10^{-11}	0.5830	0.5830	*n*-dodecane	*n*-dodecane
tridecane	13	1.68×10^{-11}	0.5465	0.5465	*n*-tridecane	*n*-dodecane
tetradecane	14	1.39×10^{-11}	0.3649	0.3649	*n*-tetradecane	*n*-dodecane
pentadecane	15	1.82×10^{-11}	0.3063	0.3063	*n*-pentadecane	*n*-dodecane
hexadecane	16	1.96×10^{-11}	0.2281	0.2281	*n*-hexadecane	*n*-dodecane
heptadecane	17	2.1×10^{-11}	0.1655	0.1655	*n*-heptadecane	*n*-dodecane
octadecane	18	2.24×10^{-11}	0.1481	0.1481	*n*-octatadecane	*n*-dodecane
nonadecane	19	2.38×10^{-11}	0.0726	0.0726	*n*-nonadecane	*n*-dodecane
eicosane	20	2.52×10^{-11}	0.0365	0.0365	*n*-eicosane	*n*-dodecane
heneicosane	21	2.67×10^{-11}	0.0222	0.0222	*n*-heneicosane	*n*-dodecane
docosane	22	2.81×10^{-11}	0.0143	0.0143	*n*-docosane	*n*-dodecane
pristane	19	2.44×10^{-11}	0.1434	0.1434	*n*-nonadecane	methylundecane
phytane	20	2.61×10^{-11}	0.0799	0.0799	*n*-eicosane	methylundecane
naphthalene	10	2.3×10^{-11}	0.1038	0.1038	naphthalene	naphthalene
phenanthrene	14	1.3×10^{-11}	0.0117	0.0117	naphthalene	naphthalene

148
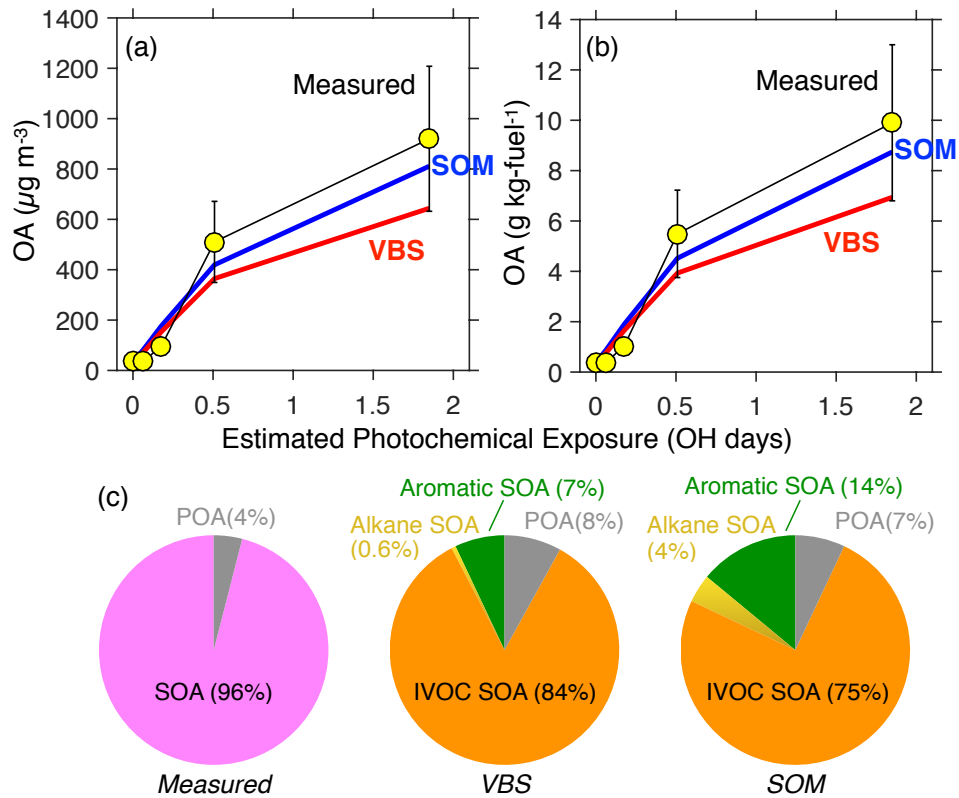
8 Figures

Figure 1: VBS and SOM model predictions of OA compared to measurements from the experiment performed on June 5 (Idle-Diesel-None) as a function of photochemical age. Inputs for both models have been specified in the text. Panel (a) has comparisons in µg m⁻³ and panel (b) has comparisons in g kg-fuel⁻¹. Panel (c) shows the modeled and measured OA composition at the highest photochemical exposure.
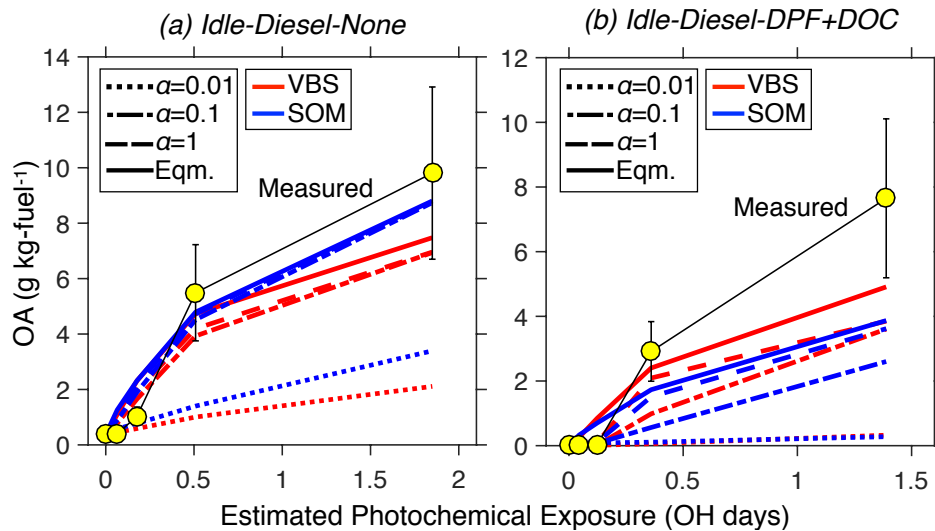
Figure 2: VBS model predictions of OA compared to measurements from the experiment performed on June 5 (Idle-Diesel-None) as a function of photochemical age assuming instantaneous equilibrium partitioning and kinetic gas/particle partitioning run at three accommodation coefficients, α = 1 (dash-dot) ,0.1 (dash) and 0.01 (solid).
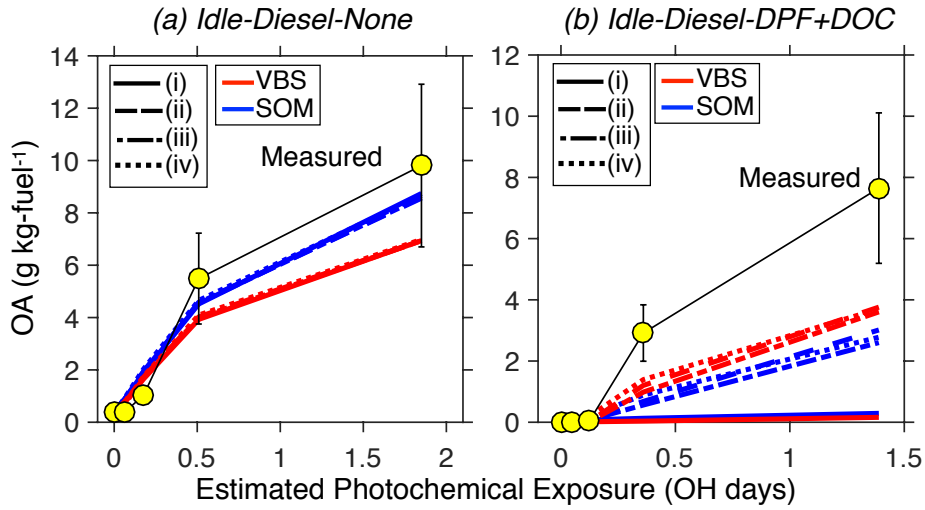
Figure 3: VBS and SOM model predictions of OA compared to measurements from the experiments performed on (a) June 5 (Idle-Diesel-None) and (b) June 11 (Idle-Diesel-DPF+DOC) as a function of photochemical age for four different particle size distribution inputs: (i) number mean diameter and measured number concentration at no OH exposure (solid), (ii) number mean diameter and measured number concentration at the given OH exposure (dash), (iii) average of (i) and (ii) (dash-dot), and (iv) nucleation of 1 nm particles (dot).
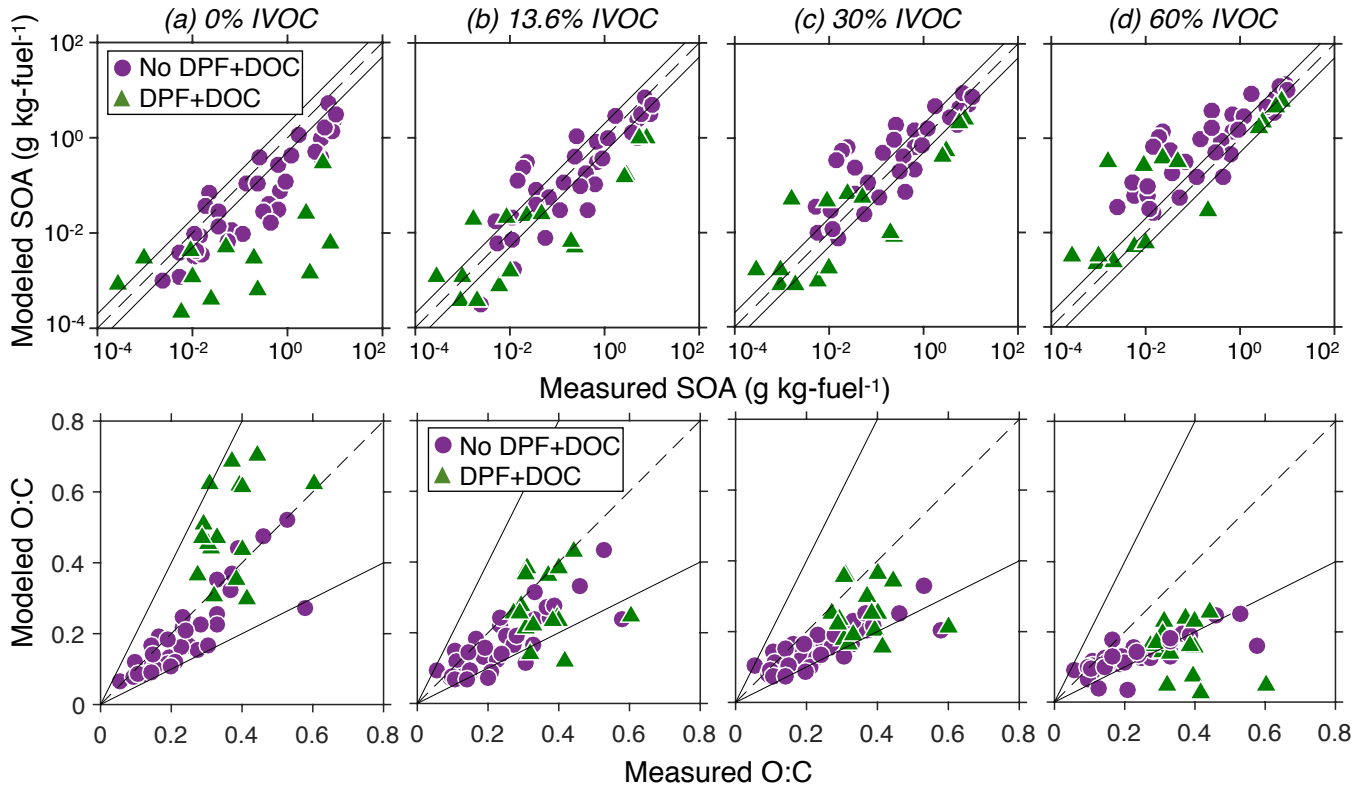
Figure 4: Scatter plot comparing SOM predictions of OA mass and O:C to measurements from all experiments at all photochemical ages at four different IVOC mass fractions: (a) 0%, (b) 13.76%, (c) 30%, and (d) 60%.
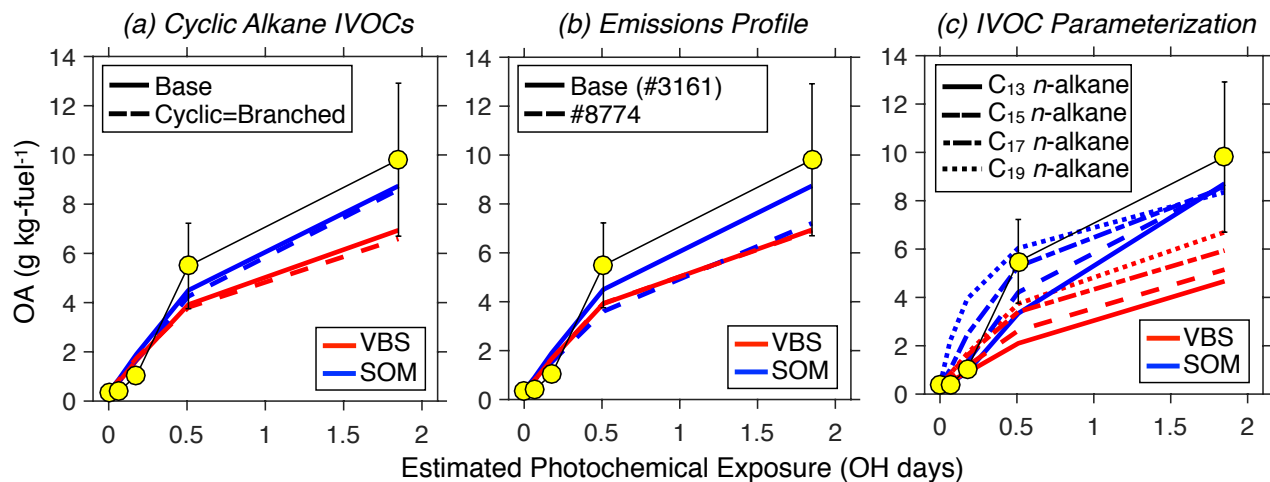
Figure 5: VBS and SOM predictions of OA compared to measurements from the experiment performed on
June 5 (Idle-Diesel-None) as a function of photochemical age. Panel (a) examines uncertainty in model
treatment of cyclic alkanes, panel (b) examines uncertainty in the VOC emissions profile, and (c) explores
suitability of using a single surrogate linear alkane to model SOA formation from all IVOCs.
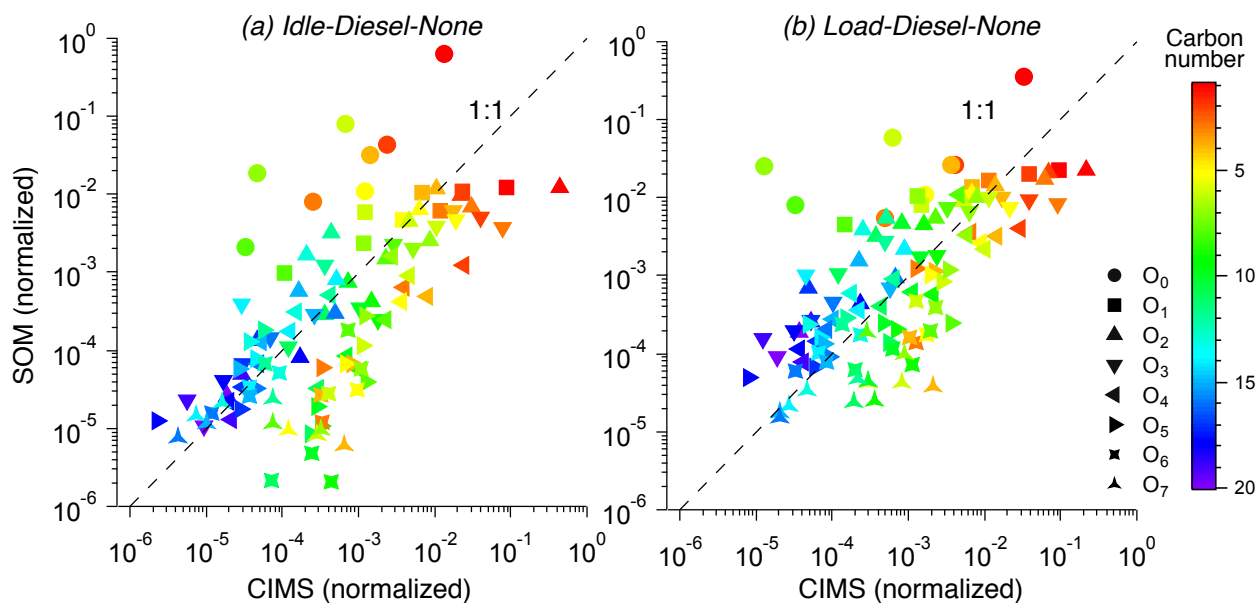
Figure 6: Normalized gas-phase concentration predictions from the SOM model for the Idle-Diesel-None
and Load-Diesel-None experiments performed on June 5 and compared to normalized gas-phase
concentrations measured by the CIMS.
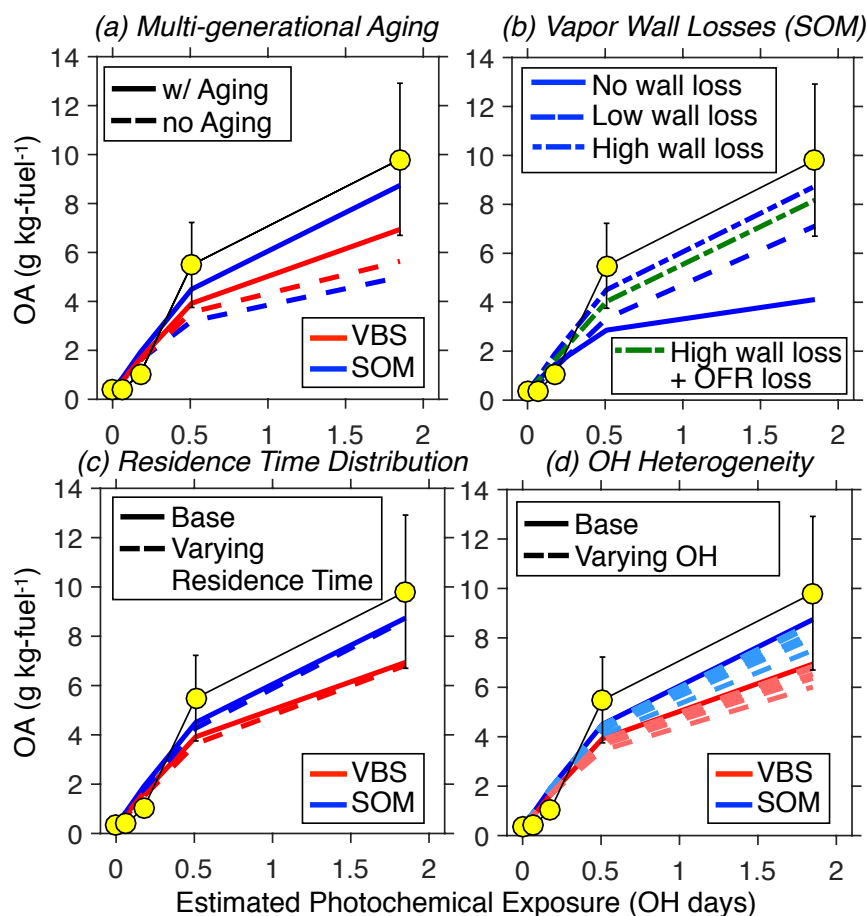
188
189 *Figure 7: VBS and SOM predictions of OA compared to measurements from the experiment performed on*
190 *June 5 (Idle-Diesel-None) as a function of photochemical age. Panels (a), (b), (c), and (d) examine the*
191 *influence of multi-generational aging, vapor wall losses, residence time distribution, and spatial*
192 *heterogeneity in OH concentrations respectively. The dashed lines in panel (d) are deliberately lighter in*
193 *color than the solid line to help differentiate the Base result from the sensitivity results.*
194
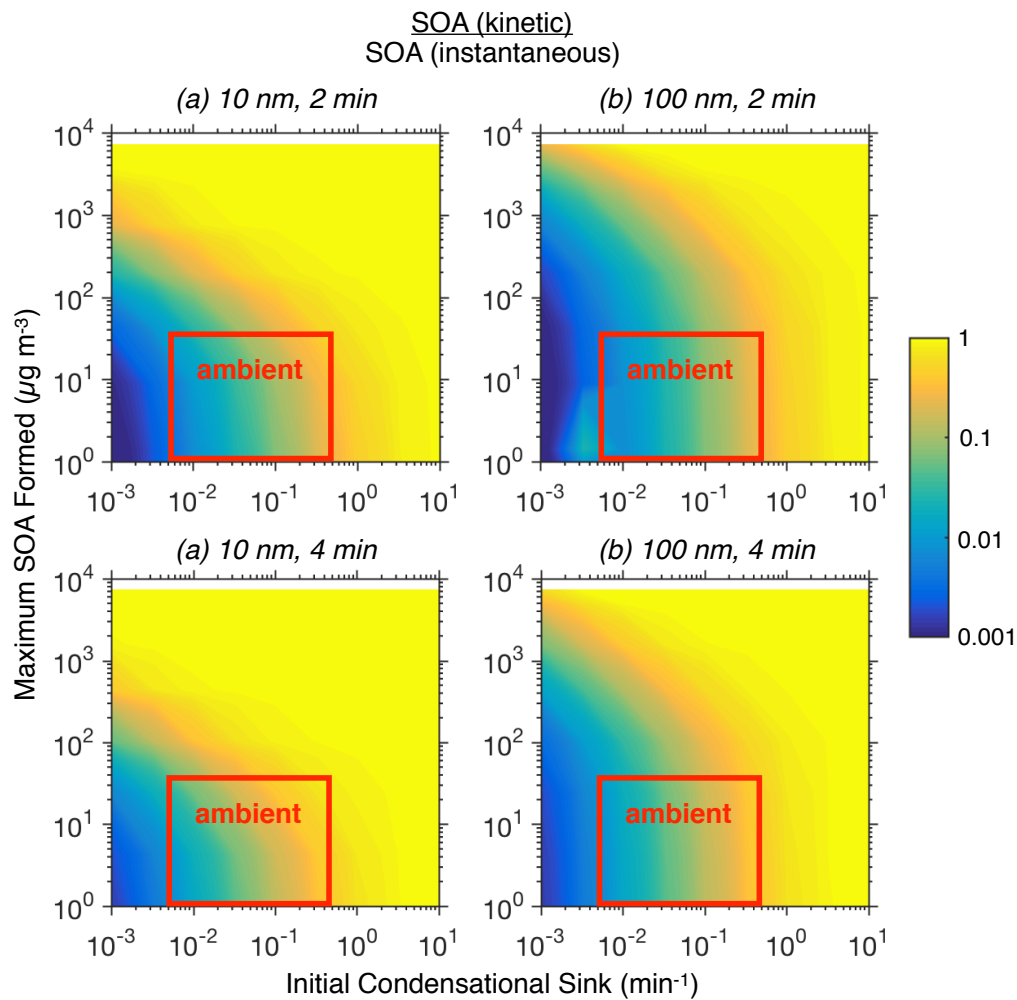
Figure 8: Model predictions of the ratio of SOA produced under kinetic partitioning assumptions to the SOA produced under instantaneous partitioning assumptions as a function of the initial condensational sink and the SOA formed under instantaneous partitioning. Panels are for calculations performed at two different particles sizes: 10 and 100 nm and two different residence times: 2 and 4 min.